Received: 12 October 2020 | Revised: 9 April 2021 | Accepted: 18 April 2021

DOI: 10.1002/qj.4046

Quarterly Journal of the Royal Meteorological Society RMetS

RESEARCH ARTICLE

Sensitivity of convective precipitation to model grid spacing and land-surface resolution in ICON

Shweta Singh | **Norbert Kalthoff** | **Leonhard Gantner**

Institute of Meteorology and Climate Research (IMK–TRO), Department Troposphere Research, Karlsruhe Institute of Technology (KIT), Karlsruhe, Germany

Correspondence
S. Singh, Institute of Meteorology and Climate Research (IMK–TRO), Karlsruhe Institute of Technology, Postfach 3640, Karlsruhe 76021, Germany.
Email: shweta.singh@kit.edu

Funding information
Federal Ministry of Education and Research (BMBF), Förderkennzeichen, Grant/Award Number: 01LK1506E

Abstract

The impact of model grid spacing and land-surface resolution (LSR) on convective precipitation are investigated for areas with different orographic complexities. ICOsahedral Nonhydrostatic (ICON) model simulations were performed for six days having weak large-scale forcing using six model grid spacings (in metres): Numerical Weather Prediction (NWP) (Δ_{5000}, Δ_{2500}) and Large-Eddy Simulation (LES) physics simulations (Δ_{1250}, Δ_{625}, Δ_{312}, and Δ_{156}) in a nested set-up. Concerning LSR, we focused on simulations with LSRs of 1,250 and 5,000 m, keeping the model grid spacing at 156 m. The onset of precipitation in Δ_{1250} is earlier by 0.5–2 hr, while LSR modifications show a similar onset compared with Δ_{156}. The relative percentage difference (RPD) of areal mean daily precipitation across LES physics simulations decreases consistently with model grid spacing for most of the cases. The RPD of precipitation in Δ_{1250} is considerably higher (75th percentile: ≈155%) than that of the LSR runs at resolutions of both 1,250 and 5,000 m, with 75th percentiles of ≈7% and ≈22%, respectively. To investigate the processes causing the differences in precipitation characteristics, like onset time and amount, the heat and moisture budgets of Δ_{1250} and Δ_{156} were compared. The results show that, at the initial stage of cloud formation, a higher number of smaller clouds are formed in Δ_{156} compared with Δ_{1250}. The small clouds in Δ_{156} are subject to considerable evaporative cooling at their edges and shell regions, due to entrainment processes. As a result, these clouds often dissolve before they can grow deep. Later on, cloud aggregation in Δ_{156} also enables precipitation. The delayed onset of precipitation and reduced areas of aggregated clouds having low precipitation rates are the main reasons for less precipitation in Δ_{156} than in Δ_{1250}.

KEYWORDS

cloud aggregation, entrainment, evaporative cooling, HD(CP)^2, ICON, LES, heat and moisture budgets

1 | INTRODUCTION

Convective precipitation is one of the more difficult phenomena to forecast in model simulations, as the processes involved range over the spatiotemporal micro- and mesoscales. Decisive processes, in particular, are convective boundary layer (CBL) turbulence, secondary circulations, and micro- and macrophysical cloud processes, as well as the conditions of the overall convective environment, the latter quantified by parameters like convective available potential energy (CAPE) and convective inhibition (CIN). Challenges in forecasting precipitation include its onset time, intensity, and spatial patterns. The simulated precipitation depends on, for example, the model grid spacing, turbulence parameterization scheme, initial and boundary conditions, and land-surface resolution (LSR).

Large-Eddy Simulation (LES) or Numerical Weather Prediction (NWP) models, which cover scales from about $\mathcal{O}$(100 m)–$\mathcal{O}$(5,000 m), on the one hand resolve deep convection (Weisman *et al.*, 1997), so that the parameterization of deep convection is not required. On the other hand, processes like turbulence and cloud microphysics still need to be parameterized over these scales: for example, from $\mathcal{O}$(100 m)–$\mathcal{O}$(1,000 m). This range is called the "grey zone" or "grey zone of turbulence" (Wyngaard, 2004; Honnert, 2016; Honnert *et al.*, 2020). Although, in the grey zone, 1-D and 3-D turbulence parameterization schemes do not fit perfectly (Honnert, 2016), model simulations therein are useful (Zhou *et al.*, 2014), so that features ranging from submesoscale (CBL heterogeneity) to mesoscale (secondary circulations) that influence convective precipitation can be appropriately represented (Chow *et al.*, 2006; Barthlott and Hoose, 2015; Hohenegger *et al.*, 2015; Adler *et al.*, 2017; Gantner *et al.*, 2017). Nevertheless, it is important to know how moist convection and precipitation depend on model grid spacing and LSR in the grey zone, as initiation and evolution of moist convection is coupled with land-surface parameters (Avissar and Chen, 1993) and their resolution (Banta, 1990; Weckwerth, 2000). Up to now, several studies have investigated the influence of model set-up and configuration on the behaviour of CBL, clouds, moist convection, and precipitation across scales of deca- and hectometres to a few kilometres, and provide possible limitations over these scales (Stevens *et al.*, 2020). For example, Efstathiou and Beare (2015) and Simon *et al.* (2019) show that grid spacing in the grey zone impacts CBL properties, such as temperature profiles. Morrison, (2016; 2017) demonstrate, based on analytical solutions and modelling, that the structure and evolution of updraughts depends considerably on model grid spacing. Hanley *et al.* (2015) tested the sensitivity of properties of convective storms to model settings, like mixing length and vertical resolution. Bryan and Morrison (2012), Verrelle *et al.* (2015), and Keat *et al.* (2019) underline the dependence of the life cycle of convective storms, for example, initiation and precipitation amount, on model grid spacing. The organisation of convection and precipitation pattern are also found to be modified by model resolution (Fiori *et al.*, 2010; Pscheidt *et al.*, 2019). Bryan *et al.* (2003) and Varble *et al.* (2020) emphasise the advantage of high-resolution simulations for a better representation of deep moist convection and squall lines.

LSR also impacts CBL conditions, mesoscale flow structures, clouds, and precipitation, as it determines the distribution of land-surface parameters (orography or land-surface properties, like vegetation and soil moisture) and, by this, the partitioning of available energy at the Earth's surface into sensible and latent heat fluxes (Kalthoff *et al.*, 1999; Western *et al.*, 2002; Koster *et al.*, 2004). For example, soil-moisture anomalies having a horizontal length-scale of $\mathcal{O}$(2.5–10 km) tend to generate corresponding circulation systems (Shuttleworth, 1991; Taylor *et al.*, 2007; Gantner and Kalthoff, 2010). Soil moisture–precipitation feedback has been proven consistently in observation and model studies (Findell and Eltahir, 1997; Schär *et al.*, 1999; Pal and Eltahir, 2001). The resolution of orography also proved to impact moist convection (Heim *et al.*, 2020), as orography triggers convection via mechanically and/or thermally induced circulations (Kirshbaum *et al.*, 2018). Chow *et al.* (2019) mention the strong interplay between the resolution of orography and precipitation in the grey zone. Imamovic *et al.* (2017) investigated the collective impacts of orography and soil moisture and found that the influence of mountains dominates once the mountain exceeds a critical height. As model grid spacing has decreased in operational forecasts in the past, even from a few kilometres to hectometres, it is important to know whether, and which, land-surface parameters are necessarily needed at a corresponding LSR. Thus, it is interesting to know how the impacts of model grid spacing and LSR compare with respect to triggering of convection, onset, and spatial distribution of clouds and precipitation, as well as precipitation intensity.

ICOsahedral Nonhydrostatic (ICON) is a new unified model system, which is now operational at Deutscher Wetterdienst (DWD) (Zängl *et al.*, 2015). It is designed for three important physics modes: that is, ICON-ECHAM, ICON-NWP, and ICON-Large Eddy Model (LEM). ICON-LEM was developed within the framework of HD(CP)^2 (Dipankar *et al.*, 2015; Heinze *et al.*, 2017; Stevens *et al.*, 2020) to understand the processes of clouds and precipitation using high-resolution modelling at a scale of up to $\mathcal{O}$(100 m). This capability enables us to apply the ICON-LEM model to simulate clouds and precipitation with grid spacings ranging from scales of $\mathcal{O}$(5,000 m) down to $\mathcal{O}$(100 m). The results provide useful information

on the model performance, as little is known up to now about how the model behaves concerning the representation of convective precipitation across these scales. The scientific objectives addressed here are as follows: to investigate and compare the impact of model grid spacing and LSR on clouds and precipitation for different types of land-surface heterogeneity (flat terrain, isolated mountain ridge, mountainous terrain). To determine the processes causing different precipitation behaviour across the model grid spacings, the heat and moisture budgets were calculated. Notably, this study is not a model evaluation but an intramodel comparison.

The outline of this article is as follows: the methodology (Section 2) explains the criterion used in this study for the selection of suitable areas and cases followed by a description of the ICON model set-up, the simulation strategy and the analysis tools. Section 3 gives an overview of the areal mean precipitation amount (Section 3.1) and the differences in onset time of clouds and precipitation, and precipitation intensity (Section 3.2) across the selected range of model grid spacings and LSRs from all cases. In Section 4, a case study is shown, using heat and moisture budgets to explain the reasons for the differences in the precipitation characteristics generated due to different model grid spacings. Finally, Section 5 summarises the overall findings of this investigation.

2 | METHODOLOGY

2.1 | Investigation areas and selected cases

Given the intention to investigate the dependence of convective precipitation on model grid spacing and LSR, we selected suitable geographical areas and days under the following specifications: (a) the areas should be distinct in terms of land-surface parameters (vegetation, soil type, orography), (b) statistically, they should be identified by considerable convective activity, and (c) the selected days should be characterised by weak synoptic forcing to allow local initiation of convection as the main source of triggering mechanism for the investigated precipitation.

To identify areas often affected by deep convection in Germany, the number density of lightning strikes for the summer period (MJJAS) from 2000–2018 was analysed, considering lightning to be a proxy of deep convection (Leary and Ritchie, 2009). The lightning data are retrieved from the Siemens lightning information service (BLIDS), which is part of the European Cooperation for Lightning Detection (EUCLID: Schulz *et al.*, 2016). As is well known from previous studies for Germany (Kottmeier *et al.*, 2008; Barthlott and Kalthoff, 2011; Kalthoff *et al.*, 2011), deep convection occurs preferentially over higher orographic terrain (Figure 1). Based on the complexity of orography (Figure 1a) and the associated number density of lightning strikes per 25 km^2 (Figure 1b), we found three areas to be suitable for our purpose: the flat terrain around and southeast of Berlin (A1); a meso-β-sized, isolated mountain range, the Harz mountains (A2); and a complex mountainous terrain, the Black Forest and its surroundings (A3). Note that all three regions are also characterised by a considerable amount of heterogeneity concerning soil type and vegetation (not shown). Finally, the selection of days was based on the aforementioned requirements, that is, weak large-scale synoptic forcing but a considerable number of lightning strikes over the respective areas. As a proxy for weak synoptic forcing, we used a threshold for the horizontal wind speed at 850 hPa of $<10\,m{\cdot}s^{-1}$, using the ECMWF ReAnalysis (ERA) Interim data set (Berrisford *et al.*, 2011; Dee *et al.*, 2011). For sufficient convective activity, a threshold of 500 lightning strikes per 25 km^2 was specified. Using these criteria, we chose six suitable days, which are listed in Table 1.

2.2 | Model set-up

ICON with version 2.3.0-nwp2 was applied to simulate the six selected days. ICON is a nonhydrostatic, fully compressible general circulation model that has been developed at DWD and the Max Planck Institute for Meteorology (MPI-M: Dipankar *et al.*, 2015; Zängl *et al.*, 2015; Heinze *et al.*, 2017).

We intend to apply ICON with grid spacings ranging from 5,000 m down to 156 m which include the "grey zone of turbulence", that is, scales of $\mathcal{O}$(100 m) to $\mathcal{O}$(1,000 m) (Wyngaard, 2004; Honnert, 2016). For these grid spacings, there are limited studies (e.g., Honnert and Masson, 2014; Cuxart, 2015) that address the grid spacing at which an appropriate transition from 1-D to 3-D turbulence schemes should be performed. The choice of turbulence schemes in this study is based on a few tests and additionally on the objective that the comparison is performed over a broader range of grid spacings (Δ_h) with the same turbulence closure, to avoid both impacts on precipitation—model grid spacing and turbulence closure—being active at the same time. Therefore, the transition in turbulence closure is done for model grid spacings $\leqq \Delta_{1250}$. For grid spacings $\leqq \Delta_{1250}$, the 3-D turbulence scheme based on the extended Smagorinsky model (Lilly, 1962) was applied (hereafter referred to as LES physics simulations, as named in Dipankar *et al.*, 2015), while, for grid spacings $> \Delta_{1250}$, the 1-D prognostic turbulent kinetic energy (TKE) based turbulence scheme described by Raschendorfer (2001a) was used (hereafter referred to as NWP physics simulations).

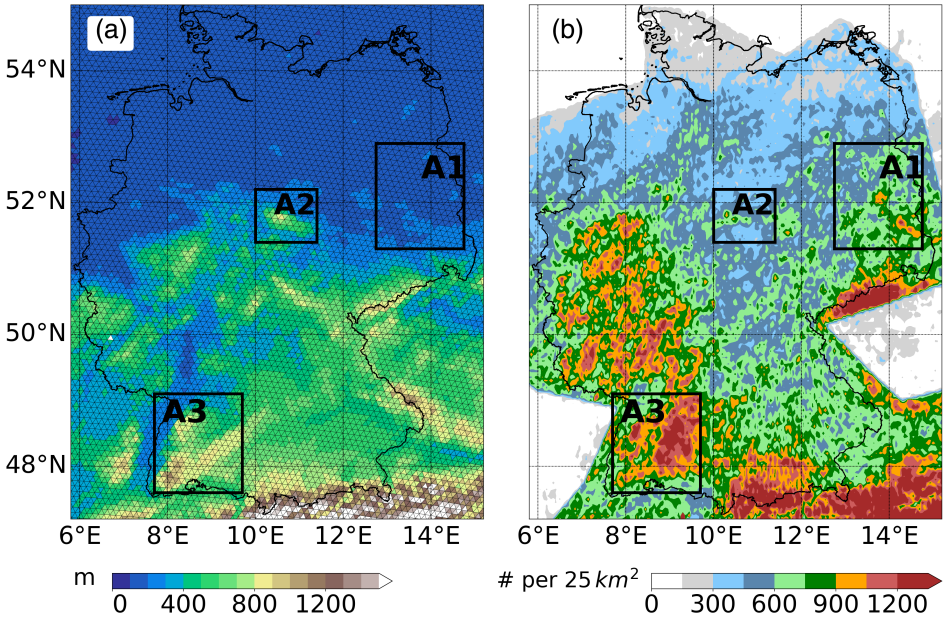

FIGURE 1 (a) Orography map with the selected areas: A1 (flat terrain), A2 (isolated mountain range), and A3 (complex terrain), and (b) total flash density during MJJAS of 2000–2018. The triangles on the orography map show the ICON-EU grid. The thin solid line marks the national boundary of Germany [Colour figure can be viewed at wileyonlinelibrary.com]

TABLE 1 Outline of simulated cases

Areas	A1: Flat terrain	A2: Isolated mountain range	A3: Complex terrain
Cases	July 26, 2012	June 09, 2018	August 12, 2015
	September 17, 2017	September 17, 2017	May 29, 2017
Model grid spacing	5,000, 2,500, 1,250, 625, 312, 156 m		
Duration	0000–2400 UTC	0000–2400 UTC	0000–2400 UTC
Initial condition	COSMO-DE and ECMWF-IFS	ICON-EU	ICON-EU
	ICON-EU	ICON-EU	ICON-EU
Boundary condition	ECMWF-IFS	ICON-EU	ICON-EU
	ICON-EU	ICON-EU	ICON-EU

At all grid spacings, the model is convection-permitting and convection parameterization was turned off.

The ICON simulations were performed in the limited-area mode. The different model grid spacings were used in a one-way nested set-up, with a local two-step grid spacing refinement, starting from the parent domain with a grid spacing of 5,000 m and going to the innermost domain at 156 m, in the ratio of two. A typical example of the domain configuration for a case simulated over flat terrain (A1, July 26, 2012) is shown in Figure 2. The set-up uses 90 vertical levels with a model top height of 20 km and lowermost minimum layer thickness of 10 m, which results in a stretching factor of model levels equal to 0.9. In order to investigate the sensitivity of the model output to model levels, additionally, tests with 150 vertical levels have been performed for a case over complex terrain (A3).

The initial and lateral boundary conditions for ICON simulations, due to availability reasons, were taken from different types of model. Out of the six cases, one case over flat terrain (A1, July 26, 2012) was initialised using the surface fields from COnsortium for small-scale MOdelling (COSMO)-DE (grid spacing of 2.8 km) and atmospheric fields from ECMWF Integrated Forecasting System (ECMWF-IFS: grid spacing of 9 km), and is relaxed towards six-hourly ECMWF-IFS analysis in a 20-km wide nudging zone. The other cases used the operational ICON analysis product ICON-Europe (ICON-EU, source: DWD-PAMORE, 2015) for initial and boundary conditions having a grid spacing of 6.5 km and 60 vertical layers. The boundary of the parent domain (Δ_{5000}) is relaxed towards three hourly ICON-EU assimilation forecast products. The source of the time-invariant data used at the lower boundary—for example, land use (GlOBCOVER: GlobCover, 2009), orography (Advanced Spaceborne Thermal Emission and Reflection Radiometer (ASTER): ASTER, 2011), soil type (Harmonized World Soil Database (HWSD): Fischer *et al.*, 2008)—is the same

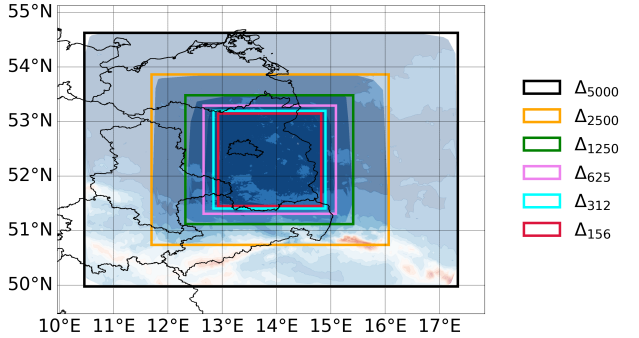

FIGURE 2 ICON model domains with different grid spacings for the flat terrain in the surroundings of Berlin (A1) for the case of July 26, 2012. This is a set-up of one-way nesting starting from Δ_{5000} nested down to Δ_{156}. The thin solid lines mark the boundaries of the federal states of Germany [Colour figure can be viewed at wileyonlinelibrary.com]

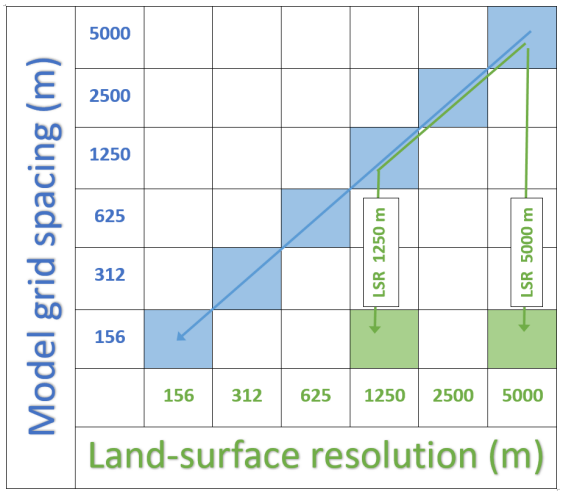

FIGURE 3 ICON simulation strategy. This outline of the model simulation strategy holds for all six cases [Colour figure can be viewed at wileyonlinelibrary.com]

as used in the ICON simulations performed in Heinze *et al.* (2017).

Regarding the model physics of these simulations, in both NWP and LES physics simulations the explicit physical processes are convection, subgrid-scale orographic effects (this controls blocking and gravity-wave drag formation), and nonorographic gravity-wave drag. The double-moment mixed-phase bulk cloud microphysics provided by Seifert and Beheng (2006) is applied. The multilayer land-surface scheme TERRA_ML (Schrodin and Heise, 2002; Heise *et al.*, 2006) is used. It forms the lower boundary condition for the atmospheric part of ICON. These ICON simulations do not use a lake or sea-ice model. Radiation is treated via the Rapid Radiation Transfer Model (RRTM: Mlawer *et al.*, 1995). The NWP and LES physics simulations differ in the treatment of the following implicit physical processes.

- Subgrid-scale turbulence scheme:
  - NWP physics simulation: Prognostic TKE COSMO (Raschendorfer, 2001b);
  - LES physics simulation: 3D Smagorinsky diffusion scheme based on Smagorinsky (1963) with the modifications by Lilly (1962) in order to consider the thermal stratification.
- Cloud cover scheme:
  - NWP physics simulation: Diagnostic Probability Density Function (PDF) cloud-cover scheme (Sommeria and Deardorff, 1977);
  - LES physics simulation: "All-or-nothing" scheme (Tompkins, 2002), which is also called a grid-scale cloud-cover scheme.

Other most relevant configurations of the model simulations are listed in Table 1.

2.3 | Simulation strategy

In accordance with the given objectives, the ICON simulations were performed with varying model grid spacings and LSRs. The corresponding simulation strategy is sketched in Figure 3. This set-up holds for all six cases. Concerning model grid-spacing experiments, six different ones (NWP physics simulations: Δ_{5000}, Δ_{2500}; LES physics simulations: Δ_{1250}, Δ_{625}, Δ_{312}, Δ_{156}) were used. These simulations are denoted as control runs (the boxes along the diagonal in Figure 3) in the following. Note that, in these simulations, model grid spacing and, inevitably, LSR have been changed simultaneously. To investigate the sensitivity of convective precipitation to vertical resolution of the model, a test run with 150 vertical levels was additionally performed.

In the LSR experiments, simulations have been performed keeping LSR constant at 5,000 and 1,250 m, respectively, and only changing the model grid spacing (LSR- 1250 and 5000 m in Figure 3). These simulations are named sensitivity runs. Overall, the land-surface parameters were categorised into two groups. The first group comprises parameters related to land-surface properties (denoted as L): this means plant cover, land use, the fraction of land and lake, and roughness length. The second group consists of parameters related to orography (denoted as O): for example, terrain height, slope angle, and slope azimuth. In this way, further sensitivity simulations have been performed in three

ways. Firstly, the land-surface properties and orography parameters were modified all together (the sets of simulations denoted as LO_{5000}, LO_{1250}). Secondly, only the land-surface properties were modified, but the resolution of orography-related parameters is the same as the corresponding model grid spacing (denoted as L_{5000}, L_{1250}). Thirdly, the orography-related parameters were modified, but the resolution of land-surface properties is used as the corresponding model grid spacing (denoted as O_{5000}, O_{1250}). Therefore the land-surface properties (L) and orography-related (O) parameters are coarsened sequentially, while the model grid spacing and atmospheric variables remain at high resolution. This is done by using the barycentric interpolation method of DWD-ICON-tools (Prill, 2014). In further investigations of the impacts of model grid spacing and LSR, we will only compare the results determined by Δ_{156} with those of the LSR sensitivity runs, having a model grid spacing of 156 m and LSRs of 1,250 and 5,000 m, respectively. For these LSR sensitivity runs the model grid spacing is the same (156 m). For the sake of simplicity, they are only indicated by the resolution of the land-surface properties and/or orography, for example, LO_{1250} and LO_{5000}, in the following analysis. Note that, for area A1, only LO simulations were performed, as orography is not considerably heterogeneous in this region.

2.4 | Analysis tools

The processes causing differences across LES physics simulations were investigated using heat and moisture budgets. The budget components have been implemented in ICON in online mode. These corresponding budget terms specify the contribution of the different components (for example, heat advection, phase change, radiative cooling/heating, turbulent mixing, etc.) to the tendencies of heat (θ_v) and moisture (q_v) (e.g., Stull, 1988; Grams *et al.*, 2010; Adler *et al.*, 2011). The different heat and moisture budget components are given in Equations 1a and 1b, respectively:

$$SUM_{\theta_v} = ADV_{\theta_v} + RAD_{\theta_v} + MICR_{\theta_v} + TURB_{\theta_v}, \quad (1a)$$

$$SUM_{q_v} = ADV_{q_v} + MICR_{q_v} + TURB_{q_v}, \quad (1b)$$

where SUM_{θ_v} (SUM_{q_v}) represents the net temperature (moisture) tendency. $MICR_{\theta_v}$ ($MICR_{q_v}$) represents the contribution of microphysics to SUM_{θ_v} (SUM_{q_v}); in other words, it is the net body source term associated with the phase changes. $TURB_{\theta_v}$ ($TURB_{q_v}$) represents the divergence of kinematic heat (moisture) flux, which describes the contribution of the parameterized turbulence to SUM_{θ_v} (SUM_{q_v}). ADV_{θ_v} (ADV_{q_v}) shows the advection of temperature (moisture) by the mean wind (horizontal and vertical). RAD_{θ_v} indicates the contribution by net radiation (shown here as the sum of net shortwave, $RADSW_{\theta_v}$, and net longwave radiation, $RADLW_{\theta_v}$) to SUM_{θ_v}.

Furthermore, the cloud-size distribution was calculated using the Python wrapper for OpenCV (Bradski, 2000). Cloud-size distributions were diagnosed based on the equivalent diameter, which is the diameter of a circle with surface area equal to the respective contour area of the cloud. Using the same wrapper, the Convective Organisation Potential (COP) (Equation 2, see also White *et al.*, 2018) was calculated to quantify cloud aggregation. COP quantifies the degree of clustering of objects (in this case clouds). It is an "all-neighbour distances" based index and holds the interaction potential between the objects ($V(i,j)$):

$$COP = \frac{\sum_{i=1}^{N}\sum_{j=i+1}^{N} V(i,j)}{\frac{1}{2}N(N-1)}, \quad (2)$$

where

$$V(i,j) = \frac{(\sqrt{A(i)} + \sqrt{A(j)})}{(d(i,j)\sqrt{\pi})},$$

$A(i)$ and $A(j)$ are the areas of objects i and j, respectively, and $d(i,j)$ is defined as the Euclidean distance between the centroids of these objects. The higher the value of the COP, the higher the degree of organisation of clouds.

Although this study focuses on the intercomparison of simulated precipitation at different model grid spacings and LSRs, rather than on a validation against observations, we also looked at the temporal evolution and spatial distribution of measured precipitation. For this, we used composites of the radar online adjustment (RADOLAN)-RW product (Bartels *et al.*, 2004) from DWD. The RW product gives radar-based quantitative precipitation estimations at a spatial resolution of $1 \times 1\,km^2$ and a temporal resolution of 1 hr covering all hydrological catchment areas of Germany. These are based on the combination of quantitative measurements with C-band Doppler radar and hourly raingauge measurements.

Moreover, the important convection indices used in the analysis are convective available potential energy of the mean surface-layer parcel (MLCAPE) and convective inhibition of the mean surface-layer parcel (MLCIN) (Doswell III and Rasmussen, 1994; Emanuel, 1994). The MLCAPE and MLCIN use the thermodynamical properties (mean temperature and humidity) of the lowest layer (50 hPa $\approx$ 500 m) in the planetary boundary layer.

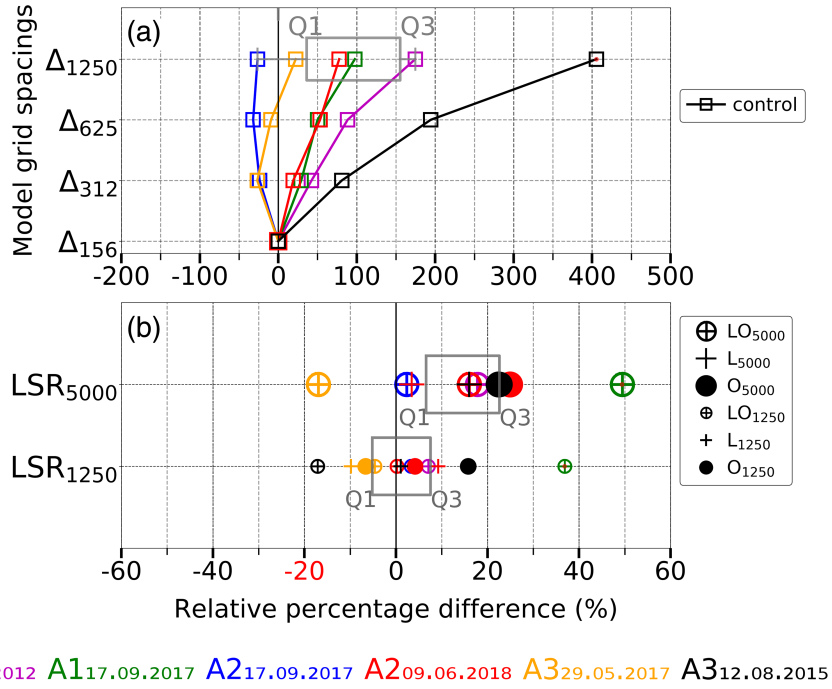

FIGURE 4 RPD of areal mean daily precipitation amount across (a) LES physics simulations (Δ_{1250}, Δ_{625}, Δ_{312}, Δ_{156}) of the control runs (□), and (b) sensitivity runs (at model grid spacing of 156 m and for LO_{1250} (⊕), L_{1250} (+), O_{1250} (●), LO_{5000} (⊕), L_{5000} (+), and O_{5000} (●) for the six simulated cases. Q1 and Q3 represent the first (25th) and third quartiles (75th percentiles) [Colour figure can be viewed at wileyonlinelibrary.com]

TABLE 2 The areal mean daily precipitation amount in control runs and RADOLAN of different cases

Cases	Areal mean daily precipitation amount (mm) in control runs and RADOLAN. Numbers in brackets are from the simulation with 150 vertical levels						
	Δ_{5000}	Δ_{2500}	Δ_{1250}	Δ_{625}	Δ_{312}	Δ_{156}	RADOLAN
A1 (July 26, 2012)	2.50	1.58	2.25	1.55	1.17	0.82	1.35
A1 (September 17, 2017)	2.51	2.81	2.36	1.80	1.55	1.20	0.02
A2 (September 17, 2017)	5.00	3.96	2.27	2.10	2.35	3.08	2.56
A2 (June 09, 2018)	1.07	1. 17	1.62	1.39	1.08	0.91	2.87
A3 (May 29, 2017)	3.22	2.21	2.48	1.84	1.48	2.03	1.36
A3 (August 12, 2015)	0.00 (0.00)	0.00 (0.20)	1.17 (1.00)	0.68 (0.61)	0.42 (0.39)	0.24 (0.21)	1.52

3 | AN OVERVIEW OF PRECIPITATION CHARACTERISTICS: ALL CASES

3.1 | Areal mean daily precipitation amount

The overview of the precipitation derived from the simulations with different model grid spacing but the same turbulence scheme (LES physics simulations) for all cases is shown in Figure 4a. It presents the relative percentage difference (RPD) of the areal mean daily precipitation amount with respect to the corresponding Δ_{156} for the set of LES physics simulations (Δ_h). We used the finest grid spacing (Δ_{156}) as the reference (Table 2). Based on all cases, the mean differences between the areal mean daily precipitation of LES physics simulations and observations are −0.23 mm at Δ_{156}, −0.27 mm at Δ_{312}, −0.05 mm at Δ_{625}, and +0.4 mm at Δ_{1250}, with standard deviations of the order of 1.2 mm. The mean differences and standard deviations of NWP physics simulations are even higher (≈ 0.55 mm and ≈ 1.8 mm, respectively). Table 2 also includes the result of the test run with an increased number of vertical levels, performed for area A3 (numbers in brackets), and shows that the sensitivity of daily precipitation to vertical resolution of the model is less in comparison with model grid spacing.

In Figure 4, a positive (negative) RPD value means that the areal mean daily precipitation amount at the given grid spacing is above (below) Δ_{156} of the respective case. The results show that the RPD of the areal mean daily precipitation amount decreases consistently with finer

model grid spacing, that is, from Δ_{1250} to Δ_{156}. Exceptions are the cases in A2 (September 17, 2017) and A3 (May 29, 2017), where Δ_{156} produce precipitation slightly higher than or similar to the other grid spacings. Overall, the variability of the areal mean precipitation in Δ_{1250} relative to Δ_{156} is considerable, ranging from −26 to 400% with third quartile (75th percentile), Q3, of 155% (Figure 4a). The resulting offset in model behaviour indicates that there is a lack of convergence in simulated mean precipitation or even cloud-system properties, at least for model grid spacings ranging from Δ_{156} to Δ_{1250}. The nonconvergent behaviour of simulated deep convection at grid spacings at 250 and 125 m was also demonstrated by, for example, Bryan *et al.* (2003) using idealized simulations of squall lines.

Comparison of the areal mean daily precipitation amount from NWP (Δ_{2500}, Δ_{5000}) with LES physics simulations shows that there is no systematic behaviour in precipitation with respect to Δ_{156} (Table 2). A case even exists where there is no precipitation in Δ_{2500} and Δ_{5000} (A3: August 12, 2015). Further insight into the different behaviours of precipitation between NWP and LES physics simulations is given in the next sections.

The RPD values of the areal mean daily precipitation amount based on LSR sensitivity runs, that is, L, O, and LO, are quite different compared with those based on changes in model grid spacing (Figure 4b). However, no systematic differences can be found when comparing the RPD values of the sensitivity runs. LO_{1250} and LO_{5000} in A1 (September 17, 2017) and A3 (May 29, 2017) result in the highest RPD values in comparison with their respective L_{1250}, O_{1250}, L_{5000}, and O_{5000}. In the case in which the LSR is smoothed down from 156 to 1,250 m (considering L, O, and LO smoothing), the RPD of the areal mean daily precipitation amount ranges from −17 to 37% with Q3 of ≈ 7% (Figure 4b). Further smoothing down the LSR from 156 to 5,000 m results in an increase in the RPD range from −17 to 49%, with Q3 equal to 22%. This means that, overall, the changes in model grid spacing (from Δ_{1250} to Δ_{156}) lead to a larger variability (Q3 ≈ 155%) in the areal mean daily precipitation amount than those caused by the LSR modifications at 1,250 and 5,000 m (Q3 ≈ 7–22%).

3.2 | Onset time, intensity, and duration of precipitation

In this section, we present more insights into the characteristics of moist convection of different LES physics simulations. In a first step, we compared the temporal evolution of clouds and precipitation. We confined the comparisons to the set of LES physics simulations of the control runs, because the differences in precipitation from the set of LSR sensitivity runs with respect to Δ_{156} are small (Figure 4). Figure 5 gives an overview of the differences in onset times of the areal mean cloud liquid water content (LWC), precipitation and precipitation intensities, and duration of Δ_{312}, Δ_{625}, and Δ_{1250} with respect to Δ_{156} for all six cases. The onset of clouds is when the rate of the areal mean of LWC, also averaged over a vertical layer of 6 km, is positive. The onset time of precipitation is defined as the time at which the areal mean precipitation amount is more than 5% of the areal mean daily precipitation amount of the corresponding Δ_{156}. The precipitation intensity is given by the accumulated precipitation amount divided by the duration of precipitation.

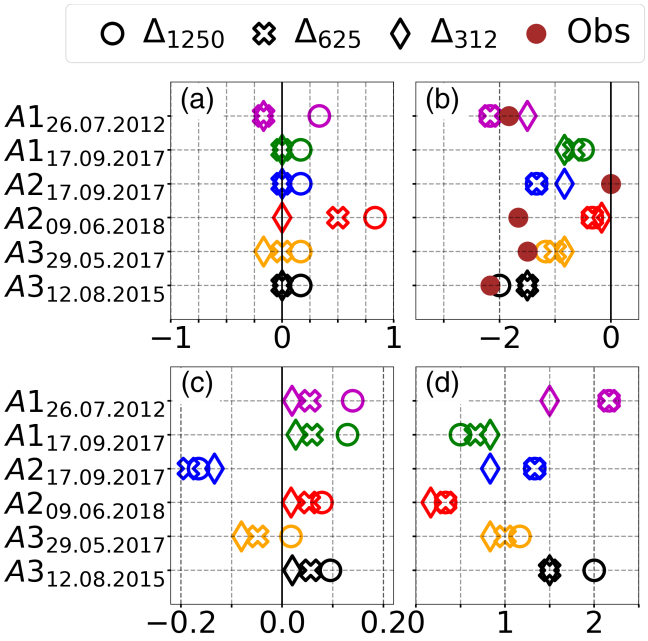

FIGURE 5 Onset time difference of (a) LWC and (b) precipitation in hours, (c) precipitation intensity difference in mm·hr^{-1}, and (d) duration difference of precipitation in hours across LES physics simulations (Δ_{1250}, Δ_{625}, Δ_{312}) and RADOLAN observation (Obs) with respect to Δ_{156}. All values are based on areal means [Colour figure can be viewed at wileyonlinelibrary.com]

The clouds formed at a similar time for most of the cases across the LES physics simulations, with an onset difference in the range of ±10 minutes with respect to Δ_{156} except for one case of A2 (June 09, 2018), where clouds are triggered earlier in Δ_{156} by 50 min compared with Δ_{1250} (Figure 5a). Overall, the clouds are triggered later in Δ_{1250} than in other LES grid spacings.

Generally, Δ_{156} always shows the latest onset time of areal mean precipitation compared with the other LES physics simulations (Figure 5b). The differences in onset times range from approximately −0.2 hr in A2 (June 9, 2018) to approximately −2.2 hr in A1 (July 26, 2012). On average, Δ_{312}, Δ_{625}, and Δ_{1250} show an earlier onset of precipitation by 0.9, 1.2, and 1.2 hr, respectively, with respect

to Δ_{156}. Note that the two cases with the largest difference in onset times, that is, A1 (July 26, 2012) and A3 (September 12, 2015), also show the greatest differences in areal mean daily precipitation amount (Figure 4b). The onsets of precipitation in the observations are mostly earlier than in Δ_{156}, ranging from 0 hr in case A2 (September 17, 2017) up to about 2 hr in case A3 (August 12, 2015). This means that the onset times of the coarser LES physics simulations fit better overall with the RADOLAN-RW data.

Figure 5c shows, that concerning the precipitation intensity difference with respect to Δ_{156}, both negative and positive values occur. The values range from $\simeq -0.19\,\mathrm{mm{\cdot}hr^{-1}}$ in A2 (September 17, 2017) to $\simeq +0.14\,\mathrm{mm{\cdot}hr^{-1}}$ in A1 (July 26, 2012). Normally, the cases showing a positive difference in precipitation intensity also correspond to a higher areal mean daily precipitation amount (A3, August 12, 2015; A2, June 09, 2018; A1, September 17, 2017; A1, July 26, 2012, Figure 4a). Thus, obviously, the differences in areal mean daily precipitation amount are mainly caused by higher precipitation intensities. The slightly negative RPD values of Δ_{1250}, Δ_{625}, and Δ_{312} in A2 (September 17, 2017) (Figure 4a) are caused by corresponding negative precipitation intensity differences (Figure 5c). The lower precipitation intensity differences of Δ_{625} and Δ_{312} values in A3 (May 29, 2017) (Figure 5c) also explain their corresponding negative RPD values (Figure 4a), while the slightly positive precipitation intensity difference of Δ_{1250} is responsible for the corresponding positive RPD value. Cases with considerably higher areal mean precipitation often also show a longer duration of precipitation (e.g., A3, August 12, 2015; A1, July 26, 2012: Figure 5d).

To summarise, for all case studies, clouds form at nearly the same time across the LES physics simulations, but for most of the cases Δ_{156} shows the latest onset of precipitation. The earlier onset time, positive precipitation intensity difference, and longer duration of the LES physics simulations (Δ_{1250}, Δ_{625}, and Δ_{312}) result in higher area mean daily precipitation amounts compared with Δ_{156}. This poses the question of why the onset of precipitation differs while the clouds form at a similar time. Case A1 (July 26, 2012) is a typical example of this kind of behaviour (Figures 4a and 5) and is therefore chosen for further investigations.

4 | CASE STUDY: A1 (JULY 26, 2012)

In this section, we analyse the spatial pattern and temporal evolution of precipitation with varying Δ_h (including LES and NWP physics simulations) and LSRs in detail for the case simulated over A1 (July 26, 2012), as this day already shows considerable RPDs in the areal mean daily precipitation amount (Figure 4a) between the LES physics simulations, for example, Δ_{1250} and Δ_{156}, as well as between their onset times, intensities, and duration (Figure 5b–d). The corresponding results for the other five cases can be found in Singh (2020).

4.1 | Temporal evolution of precipitation

As is known from Figure 4a, in the LES physics simulations, the areal mean daily precipitation amount on this day increases with coarser model grid spacing, that is, from Δ_{156} to Δ_{1250}. During the period of precipitation in all LES physics simulations, the precipitation increases nearly linearly and no significant precipitation breaks occur in between (Figure 6). However, due to different intensities (Figure 5c), their slopes increase from finer to coarser grid spacings. Although the time of first cloud formation differs only by 20 min (Figure 5a), there is a big difference in onset times of precipitation ($\approx$ 2 hr) between Δ_{156} and Δ_{1250} (Figure 5b), that is, precipitation in Δ_{1250} starts at 1130 Coordinated Universal Time (UTC), while, in Δ_{156}, precipitation onset is only at 1410 UTC. The reasons for these differences in onset times are analysed in Section 4 in more detail. Additionally, in Δ_{1250} the duration of precipitation is about 2 hr longer than in Δ_{156} (Figure 5d).

Concerning the modification in LSRs of L and O simultaneously over the scale of 1,250 and 5,000 m, this has almost a negligible impact on the onset and duration of precipitation (Figure 6). The higher areal mean daily precipitation amounts in LO_{1250} and LO_{5000}, in comparison with Δ_{156} (Figure 4b), are due to their slightly higher precipitation intensity (Figure 6). However, this range of increment in precipitation due to coarsening of LSR from 156 to 5,000 m is even smaller than that due to increasing model grid spacing from 156 to 312 m (Figure 6).

Figure 6 also includes the areal mean precipitation from NWP physics simulations (Δ_{2500} and Δ_{5000}). Both reveal a completely different behaviour in the evolution of precipitation compared with runs based on the LES physics simulations. In both NWP physics simulations, the precipitation starts even later than in Δ_{156}. In Δ_{5000}, precipitation is delayed by almost 1.5 hr compared with Δ_{156}. However, compared with the other LES physics simulations and LSR simulations, the NWP physics simulations show very high precipitation intensities, for example, precipitation intensity amounts to $\approx 0.7\,\mathrm{mm{\cdot}hr^{-1}}$ in Δ_{5000} and to $\approx 0.4\,\mathrm{mm{\cdot}hr^{-1}}$ in Δ_{2500}, whereas it is only $\approx 0.13\,\mathrm{mm{\cdot}hr^{-1}}$ in Δ_{156}.

Figure 6 also shows the time evolution of areal mean precipitation of the RADOLAN-RW product. It indicates

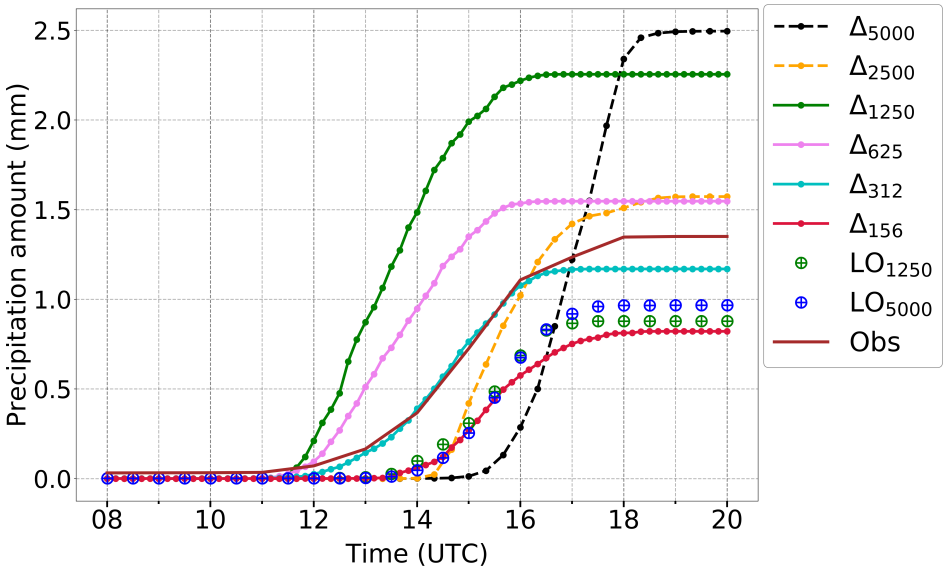

FIGURE 6 Time series of accumulated areal mean precipitation amount in NWP (Δ_{5000}, Δ_{2500}), dashed lines, and LES physics simulations (Δ_{1250}, Δ_{625}, Δ_{312}, Δ_{156}), solid lines, LO_{1250} (⊕), LO_{5000} (bigger ⊕), and RADOLAN observation (Obs) for case study A1 on July 26, 2012 [Colour figure can be viewed at wileyonlinelibrary.com]

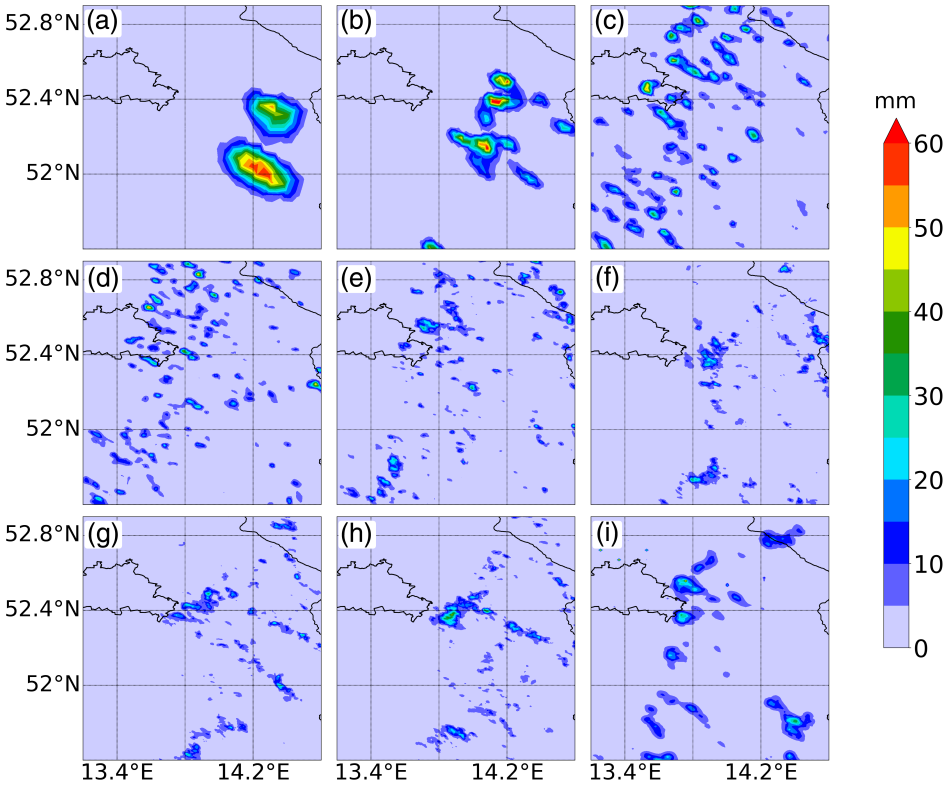

FIGURE 7 Daily precipitation amount (colour-coded) across (a,b) NWP physics simulations (Δ_{5000}, Δ_{2500}), (c–f) LES physics simulations (Δ_{1250}, Δ_{625}, Δ_{312}, Δ_{156}), sensitivity runs (g) LO_{1250} and (h) LO_{5000}, and (i) the RADOLAN observation for case study A1, July 26, 2012. The thin solid lines indicate the border of Berlin and the Germany–Poland border, respectively [Colour figure can be viewed at wileyonlinelibrary.com]

that the onset of areal mean precipitation in Δ_{1250}, Δ_{625}, and Δ_{312} is closer to observations, while the temporal evolution of Δ_{312} resembles observations better than the other LES and NWP physics simulations.

4.2 | Spatial distribution of precipitation

Figure 7 shows the spatial distribution of daily precipitation amounts from the control, the sensitivity runs (LO_{5000} and LO_{1250}), and observations of the case simulated over A1 (July 26, 2012). We see that Δ_{156} produces clustered and non-uniform precipitation patterns in the east and south-east of Berlin (Figure 7f), whereas the other LES physics simulations, that is, Δ_{1250}, Δ_{625}, and Δ_{312}, form more dispersed, but relatively uniformly sized, patches of precipitation throughout the east of Berlin (Figure 7c–e). However, there is an overall convergence of precipitation patterns with a decrease in grid spacing from Δ_{1250} to Δ_{156}, as also observed in the other five simulated cases (Singh, 2020).

It follows the previous finding of Fiori *et al.* (2010) that the model simulations with LES turbulence closure tend to converge in terms of precipitation characteristics. Δ_{1250} produces more intense patches of precipitation in comparison with finer LES physics simulations, which is a consistent model behaviour found in the precipitation patterns simulated for other cases. Furthermore, we see the impact of the two different turbulence parameterization schemes (NWP and LES) on the precipitation patterns, for example, the spatial patterns of the daily precipitation amounts differ considerably between NWP (Δ_{5000}, Δ_{2500}: Figure 7a,b) and LES physics simulations (Δ_{1250}–Δ_{156}: Figure 7c–f). The NWP physics simulations produce completely different, bigger, more isolated and more intense patches with precipitation in comparison with LES physics simulations. Larger and more intense patches of precipitation in NWP physics simulation compared with higher resolution models were also reported by Hanley *et al.* (2015). Note that the more-favoured triggering of isolated convection in NWP simulations of a case study could also result in no precipitation at all, as valid for the case simulated over the Black Forest (A3, August 12, 2015; Table 2). The 1-D prognostic TKE-based turbulent parameterization scheme with negligible contributions of horizontal turbulent mixing leads to a different forcing of convection, especially in complex terrain (Honnert and Masson, 2014; Couvreux *et al.*, 2016; Rotach *et al.*, 2017). A "by-eye" comparison of the simulated and observed patterns suggests that Δ_{312} and Δ_{156} fit best with the observations (Figure 7i), while NWP simulations show the greatest differences from the observations. This conclusion generally holds for the other five cases (Singh, 2020).

Regarding the impact of LSR on precipitation, Figure 7g,h shows the spatial pattern of the daily precipitation amount based on the LO_{5000}, LO_{1250} simulations. The spatial distributions of the precipitation patterns of both simulations are quite similar to Δ_{156} (Figure 7f), except for some minor differences, like the clustered precipitating pattern in the east of Berlin, which at least in LO_{5000} is relatively bigger in size than the one in Δ_{156}. This means that the small differences in areal mean daily precipitation amount based on LSR modifications (Figure 4b) and model grid spacing (Figure 4a) go along with the differences in their spatial distribution.

Overall, we see a stronger impact of model grid spacing on precipitation patterns in comparison with LSR modifications on a scale of hectometres to a few kilometres, which is a consistent model behaviour analysed in the other cases and areas (Singh, 2020). Therefore, we focus further on the reasons causing the differences in precipitation due to model grid spacing.

4.3 | Conditions and processes causing the differences in precipitation

We now investigate the processes involved in causing the RPD of ≈175% in the areal mean daily precipitation amount between Δ_{156} and Δ_{1250} (Figure 4a).

With respect to the temporal evolution of precipitation in the two model grid spacings, the conditions at two times are of special interest: firstly at 1200 UTC, when precipitation started in Δ_{1250}, and secondly at 1400 UTC, when there is onset of precipitation in Δ_{156} (Figure 6). Concerning the spatial distribution, the reasons for the more clustered precipitation patterns in Δ_{156} compared with the mostly widespread distribution of precipitation in Δ_{1250} are of major interest (Figure 7c,f). The final question is what causes the differences in the areal mean daily precipitation amount. In a first step, the parameters representing the overall potential for convective activity, for example, MLCAPE and MLCIN, are investigated.

4.3.1 | Convection indices

Figure 8a shows that the areal mean MLCAPE increases more strongly in Δ_{1250} than in Δ_{156} in the morning, reaching maximum values of ≈1,300 $J \cdot kg^{-1}$ around 1000 UTC, while in Δ_{156}, it is only ≈1,000 $J \cdot kg^{-1}$ at that time. The areal mean MLCIN values of ≈10 $J \cdot kg^{-1}$ and ≈15 $J \cdot kg^{-1}$ in Δ_{1250} and Δ_{156}, respectively, around 1000 UTC also indicate slightly more favourable conditions for convection in Δ_{1250} in comparison with Δ_{156}. Both factors could explain the higher areal mean daily precipitation amount in Δ_{1250} than in Δ_{156} (Emanuel, 1994). The spatial distributions of the convection indices at 1000 UTC, that is, the time of first cloud formation, show that neither quantity is distributed homogeneously over the investigation area, but MLCAPE has a maximum and MLCIN has a minimum along a stripe oriented from southwest to northeast (Figure 9). This finding is valid for both Δ_{156} and Δ_{1250}—although with relatively more structure in Δ_{156}—and explains the evolution of precipitation primarily in this southwest to northeast oriented stripe (Figure 7c–f).

4.3.2 | Boundary layer and cloud characteristics

To elucidate the different development of convection parameters, clouds, and precipitation in Δ_{156} and Δ_{1250}, more in-depth analysis based on macrophysical cloud parameters as well as budget studies of heat and moisture was performed. Before cloud formation, for example,

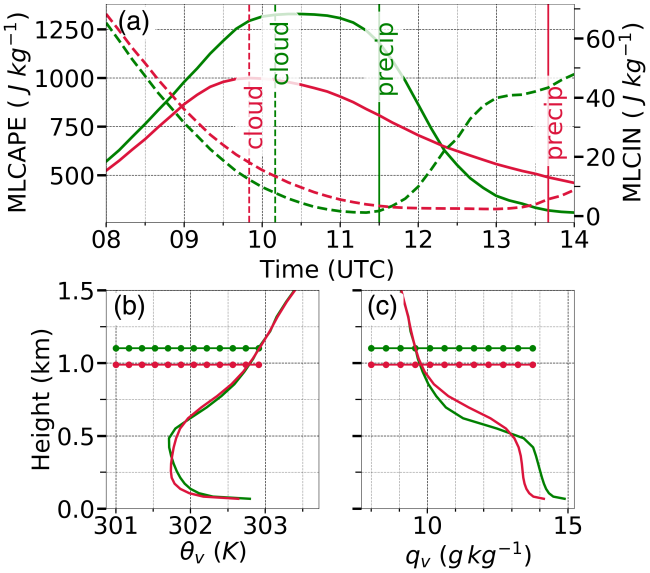

FIGURE 8 (a) Temporal evolution of areal mean MLCAPE (solid curve) and MLCIN (dashed curve) for Δ_{1250} (green) and Δ_{156} (red). Vertical dashed lines indicate first evolution of clouds and solid lines first onset of precipitation in Δ_{1250} (green) and Δ_{156} (red), respectively. (b) Vertical profiles of areal mean virtual potential temperature (θ_v) and (c) specific humidity (q_v) in Δ_{1250} (green curve) and Δ_{156} (red curve) at 1000 UTC for the case simulated over A1 (July 26, 2012). The horizontal lines with circle markers denote the areal mean CBL height (z_i) [Colour figure can be viewed at wileyonlinelibrary.com]

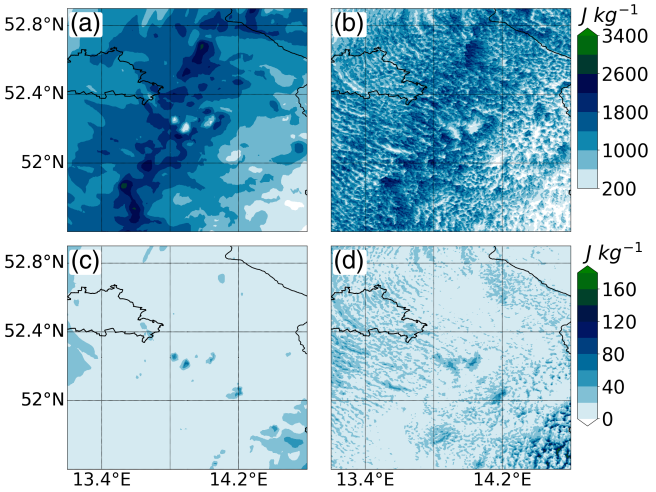

FIGURE 9 Spatial distribution of MLCAPE and MLCIN at 1000 UTC for (a,c) Δ_{1250} and (b,d) Δ_{156}, respectively, for the case simulated over A1, July 26, 2012. The thin solid lines indicate the border of Berlin and the Germany–Poland border, respectively [Colour figure can be viewed at wileyonlinelibrary.com]

at 1000 UTC, Δ_{156} produces earlier and more strongly resolved grid-scale turbulence (represented by the vertical velocity variance, $\overline{w'^2}$) in the CBL than in Δ_{1250} (Figure 10a,b). In Δ_{1250}, no considerable resolved convection is present in the CBL at that time (Figure 10a). This means that the rate of partitioning of the total turbulent fluxes into resolved (grid-scale) and parameterized (subgrid-scale) fluxes is rather different in Δ_{156} and Δ_{1250}. The stronger effective vertical mixing of heat and moisture in Δ_{156} than in Δ_{1250} has a considerable impact on the resulting profiles of θ_v and q_v (Figure 8b,c). Δ_{1250} results in a warmer and moister condition in the lowest ≈300 and 500 m layers, respectively, in comparison with Δ_{156}. Such an influence of grid spacing on vertical mixing and stratification in the CBL was also described by Simon *et al.* (2019) and Efstathiou and Beare (2015), that is, potential temperature profiles become more superadiabatic with increasing grid spacing. This more unstable stratification in Δ_{1250} is responsible for higher MLCAPE and lower MLCIN values than those in Δ_{156} (Figure 8a), together with considerable spatial variability (Figure 9). In subsequent hours, CBL clouds form in both model grid spacings (Figure 10a,b). However, for example, until 1200 UTC, under more favourable convective conditions, the clouds grow deeper in Δ_{1250} (≈ 10,000 m) in comparison with Δ_{156} (≈ 6,100 m) (Figure 9).

4.3.3 | Heat and moisture budgets

Insight into the processes relevant to the different behaviours for the period between 1000 and 1200 UTC, when CBL clouds grow into deep convection, can be gained by analysing the areal mean heat and moisture budgets (notations of the different budget components are given in Section 2.4). As stated, Δ_{156} at 1200 UTC shows no precipitation, whereas Δ_{1250} simulates these 10,000 m deep clouds (Figure 10) and already some precipitation (Figure 6). Therefore, we compare the heat and moisture budgets at this time step for both model grid spacings.

In Δ_{156} in the subcloud layer at 1200 UTC, SUM_{θ_v} with a value of ≈0.5 K·hr^{-1} is relatively constant with height (Figure 11b). As is typical of convective conditions, positive values of RAD_{θ_v} and $TURB_{\theta_v}$ contribute to SUM_{θ_v} in the lowest ≈ 200 m. ADV_{θ_v} causes cooling in the lower part and heating in the upper part of the subcloud layer. This heat exchange between the two layers is mainly taken over by grid-scale vertical heat fluxes (not shown), as convection is well resolved in Δ_{156} (Figure 10b). Concerning the moisture budget, the net moisture decreases in the lower part and increases in the upper part of the subcloud layer (Figure 11d). Two processes contribute to SUM_{q_v}. $TURB_{\theta_v}$ feeds moisture into the lower part of the subcloud layer, while ADV_{q_v} contributes to the moisture exchange between the lower and upper parts of the subcloud layer

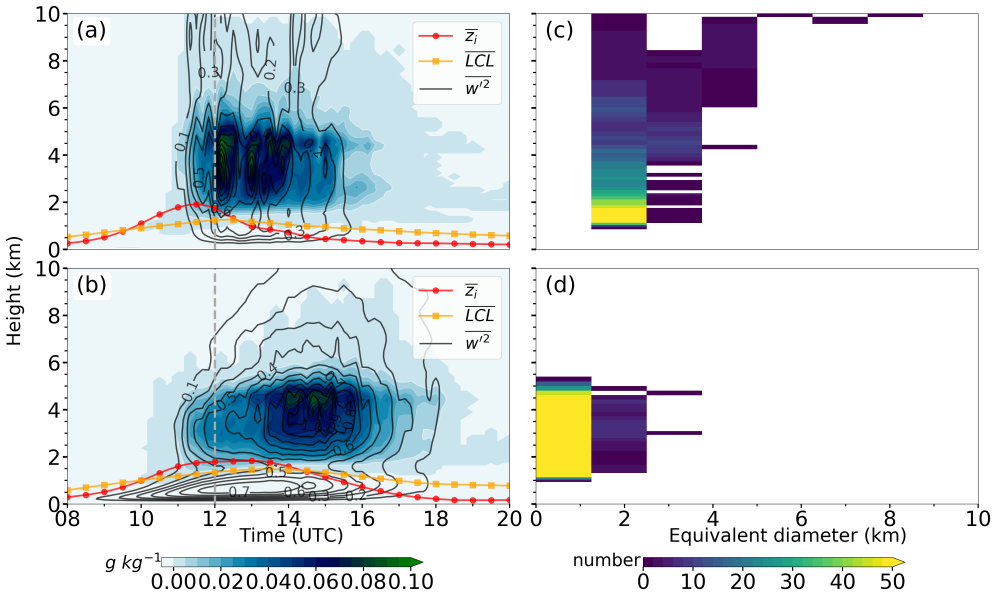

FIGURE 10 Time–height cross section of areal mean LWC, q_c, (colour-coded) overlaid with vertical wind variance, $\overline{w'^2}$ (black contours) in (a) Δ_{1250} and (b) Δ_{156}, respectively, for the case study A1, July 26, 2012. The horizontal curves with circle and square markers denote areal mean CBL height (z_i) and lifting condensation level (LCL), respectively. Number concentration of cloud equivalent diameter with respect to height is shown at 1200 UTC for (c) Δ_{1250} and (d) Δ_{156}, respectively [Colour figure can be viewed at wileyonlinelibrary.com]

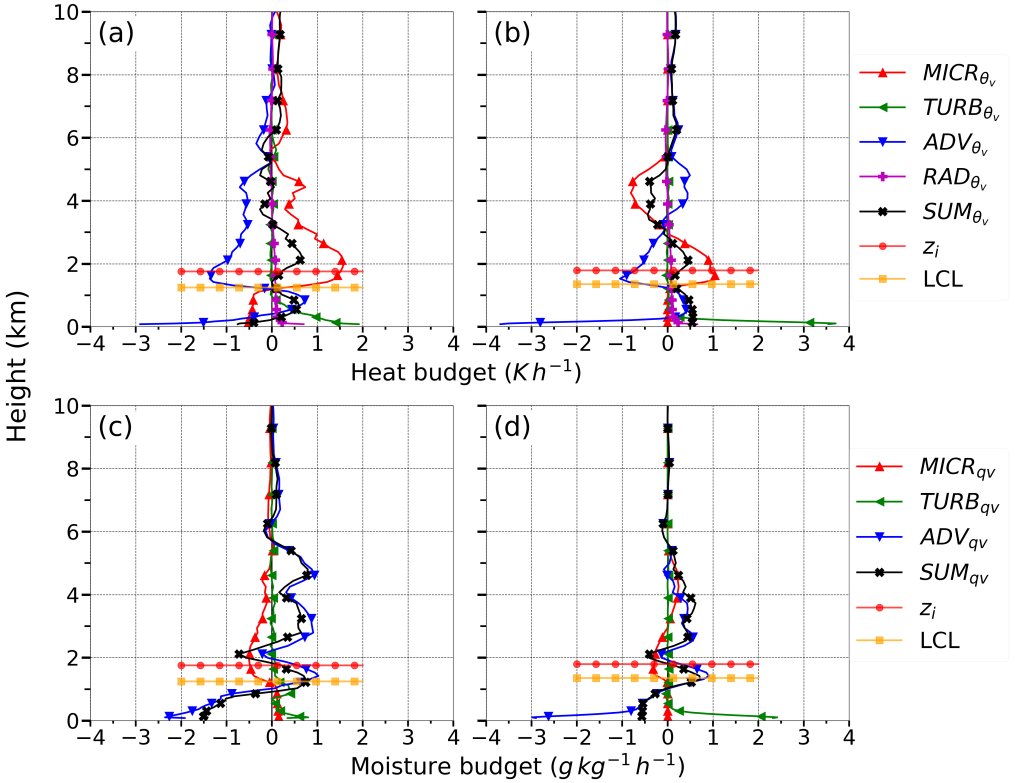

FIGURE 11 Vertical profiles of areal mean heat and moisture budget terms within the CBL and free troposphere in (a,c) Δ_{1250} and (b,d) Δ_{156} at 1200 UTC for case study A1, July 26, 2012. The horizontal with square and circle indicate the areal mean LCL and CBL height (z_i), respectively [Colour figure can be viewed at wileyonlinelibrary.com]

and also to the lower cloud layer. Similarly to the heat budget, the moisture exchange is due mainly to grid-scale vertical moisture fluxes (not shown). In Δ_{1250} in the subcloud layer at 1200 UTC, the contributions of the different terms to the heat and moisture budget, in general, are quite similar to the ones in Δ_{156}, but with a difference in amounts (Figure 11). For example, due to the evaporation of rain in the subcloud layer, $MICR_{\theta_v}$ causes cooling there (≈ -0.6 K·hr^{-1}). Therefore, net heating is restricted to the upper part of the subcloud layer (Figure 11a) and therein at the same time the evaporation of rain contributes to a slight increase in moisture, $\approx +0.1$–0.2 g·kg^{-1} ·hr^{-1} (Figure 11c).

The largest difference between Δ_{156} and Δ_{1250} concerning processes relevant to the development of clouds and precipitation can be found in the cloud layer. In Δ_{1250}, two budget terms dominate the SUM_{θ_v} that is, $MICR_{\theta_v}$ and

ADV_{θ_v}. Condensational heating exists (positive $MICR_{\theta_v}$), reaching maximum values of up to 1.5 K·hr^{-1} in the lower part of the cloud layer (at about 2,000 m) and then degrading with height. This condensational heating, however, is mostly compensated for by negative values of ADV_{θ_v}. By investigating the spatial distribution of the budget terms, we will show later where these negative contributions are generated. Finally, the lower parts of the cloud layer show net heating ($SUM_{\theta_v} \approx 0.5$ K·hr^{-1}), while SUM_{θ_v} remains small above up to the cloud tops at about 10,000 m (Figure 11a). Similarly to the heat budget, only two terms dominate the SUM_{q_v} (Figure 11c,d). The formation of cloud water in the cloud layer results in negative contributions of $MICR_{q_v} \approx -0.5$ g·kg^{-1} ·hr^{-1} to SUM_{q_v} at 2,000 m. This process is overcompensated for by ADV_{q_v}, causing a continuous increase in moisture with values of up to $SUM_{q_v} = 0.9$ g·kg^{-1} ·hr^{-1} in nearly the whole cloud layer. As discussed with respect to the subcloud layer, the cloud layer to a large extent is fed with moisture from below.

Comparing the above budgets behaviour in Δ_{156} and Δ_{1250}, the most striking differences occur in the upper part of the cloud layer. In Δ_{156}, between ≈ 3,000 and 5,000 m a net cooling layer can be found ($SUM_{\theta_v} \approx -0.5$ K·hr^{-1}), where $MICR_{\theta_v}$ shows the dominant contribution (with a value of up to ≈ −0.8 K·hr^{-1}, Figure 11b). This net evaporation of clouds is also reflected in the moisture budget, causing a moisture increase due to $MICR_{q_v}$ of up to 0.3 g·kg^{-1} ·hr^{-1} (Figure 11d). This contribution due to evaporation of clouds adds up with the effect of moisture advection (ADV_{q_v}, which of in the order of ≈ 0.5 g·kg^{-1} ·hr^{-1}) in the upper part of the cloud layer. Hence, the major differences between the heat and moisture budget of Δ_{156} and Δ_{1250} at 1200 UTC consist of the fact that, while the cloud formation ($MICR_{\theta_v}$) in Δ_{1250} reaches from the cloud base to the cloud top up to 10,000 m, in Δ_{156} $MICR_{\theta_v}$ contributes to cloud development only in the lower half of the cloud layer (1,200–3,000 m), while contributing to cloud dissolution in the upper part of the cloud layer (3,000–5,500 m).

To understand further the different behaviours of the clouds in this layer between 3,000 and 5,500 m, the spatial distributions of $MICR_{\theta_v}$ and ADV_{θ_v} at a height of ≈ 4,000 m are investigated for Δ_{1250} and Δ_{156} (Figure 12a,b), respectively. The figure shows a zoomed view of typical clouds formed in the two grid spacings. Positive $MICR_{\theta_v}$ values indicate areas with condensational heating or latent heat release (LHR) caused by cloud formation, while negative $MICR_{\theta_v}$ is an indication of associated evaporative cooling due to the dissolution of clouds. Δ_{1250} produces bigger clouds, whereas Δ_{156} simulates several smaller clouds (see also Figure 10c,d). Though the heating due to $MICR_{\theta_v}$ in the cloud core is comparable in both grid spacings, the clouds in Δ_{156} show significantly stronger evaporative cooling at the cloud edges and shell

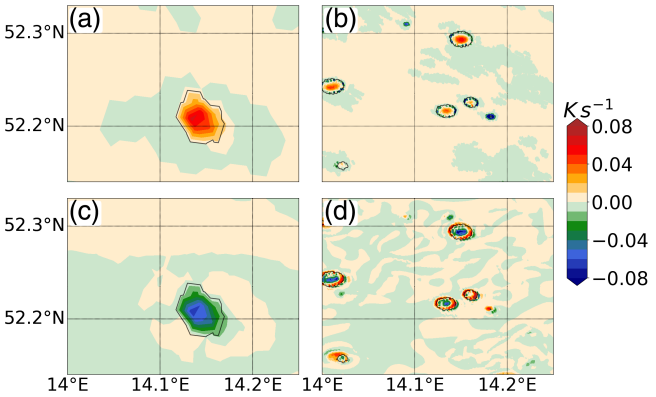

FIGURE 12 Spatial distribution of microphysics contribution to temperature tendency, $MICR_{\theta_v}$ (colour-coded), in (a) Δ_{1250} and (b) Δ_{156}, and contribution by temperature advection, ADV_{θ_v} (colour-coded), in (c) Δ_{1250} and (d) Δ_{156} at ≈ 4,000 m height at 1200 UTC for case study A1, July 26, 2012. The black contours are the isolines for LWC of 0.1 g·kg^{-1} at that level, used as proxy for the cloud areas [Colour figure can be viewed at wileyonlinelibrary.com]

regions in comparison with Δ_{1250}. In total, in Δ_{156} between 3,000 and 5,500 m evaporative cooling dominates over condensational heating ($MICR_{\theta_v} < 0$, Figure 11), which causes the dissolution of clouds, so that on average the clouds do not grow deep at that time (Figure 10b,d). This process in Δ_{156} obviously led to the delayed onset of the precipitation in Δ_{156} in comparison with Δ_{1250} (Figure 6). Figure 12c,d additionally shows the spatial distribution of ADV_{θ_v} at 4,000 m. Cooling due to warm-air advection takes place in the updraught region of the cloud cores, while warming occurs due to downdraughts in the shell regions and edges of the clouds, as the atmosphere in the free troposphere is stably stratified.

The possible cause behind the occurrence of considerable cooling along the shell region of clouds is explained using the size distribution of clouds calculated for the cloud cover simulated in Δ_{1250} and Δ_{156} (Figure 10c,d). As is evident, Δ_{156} produces a greater number of smaller and shallower clouds than Δ_{1250}, where bigger and deeper clouds prevailed. Morton *et al.* (1956) and Turner (1963) have given a quantitative description of entrainment based on laboratory water-tank experiments of thermal plumes, describing the relation between mass flux, entrainment rate, and the radius of the rising plume. According to this relation, the entrainment rate is approximately inversely proportional to the radius of the rising plume. This means that the smaller the plume, the higher the entrainment rate. Therefore, the smaller clouds in Δ_{156} are easily detrained by the dry environmental air, are prevented from growing deeper, or can even be dissolved in Δ_{156}. The entrainment causes evaporative cooling, which also reduces the buoyancy of the convective parcels. As evident from Figure 12d, the entrainment zone along the

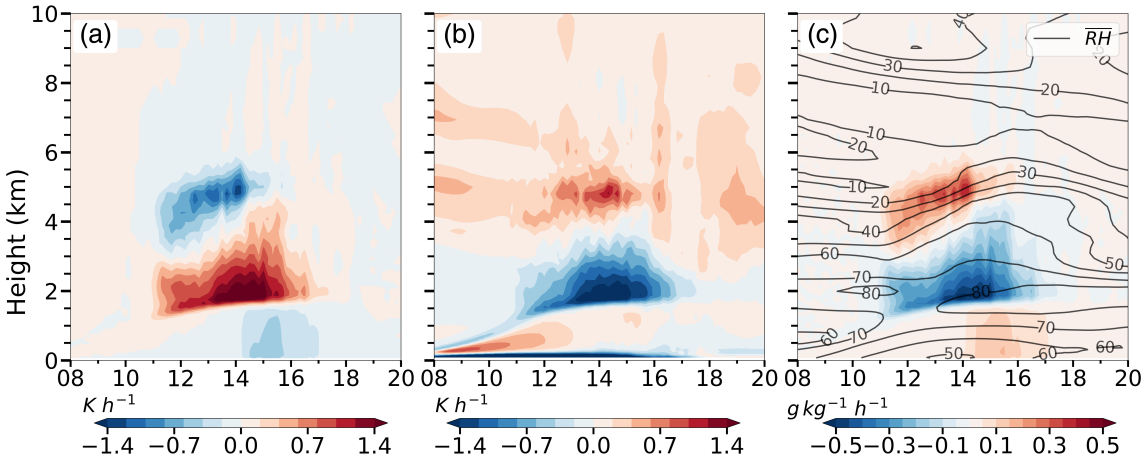

FIGURE 13 Time–height cross section of areal mean (a) $MICR_{\theta_v}$ (colour-coded), (b) ADV_{θ_v} (colour-coded), and (c) $MICR_{q_v}$ (colour-coded) overlaid with areal mean relative humidity (black isolines) in Δ_{156} for the case study A1, July 26, 2012 [Colour figure can be viewed at wileyonlinelibrary.com]

edges of the clouds consists of regions with downdraughts due to negative buoyancy. The evaporative cooling in the small-sized clouds is a prominent phenomenon analysed in Δ_{156} for other cases (Singh, 2020), resulting in the formation of detached shallow cumulus clouds. The increasing effect of cloud evaporation with decreasing grid spacing and the associated differences in the onset of precipitation were also described by, for example, Bryan and Morrison (2012) and Verrelle *et al.* (2015).However, Keat *et al.* (2019) found out an opposite behaviour, that is, 300-m grid spacing shows slightly an earlier onset of convection than 1.5-km grid spacing in the Met Office Unified model simulation. Thus, the a priori expectation that anything that makes the model fields less smooth results in an earlier onset of convective precipitation, due to being able to represent smaller initial plumes, is not necessarily fulfilled. This article finds the opposite, for the reasons elucidated related to the formation of smaller clouds in finer grid spacings. Obviously, whether the direction of the convective initiation moves as grid spacing changes is down to a balance between the factors discussed above.

As discussed in Section 3.2, precipitation in Δ_{156} occurs at about 1350 UTC, that is, more than 2 hr later than in Δ_{1250} (Figures 5b and 6). Hence, the question is: what processes allow the clouds to grow deeper after 1200 UTC and to precipitate at around 1350 UTC? As microphysics and advection were the decisive processes concerning the heat and moisture tendency at 1200 UTC (Figure 11), we focus further on the temporal development of these budget terms in the following (Figure 13). In Δ_{156}, grid-scale turbulence ($\overline{w'^2}$) in both the subcloud and cloud layers becomes stronger and reaches higher up, that is, the 0.2 $m^2 \cdot s^{-2}$ isoline increases from about 5,000 m at 1200 UTC to 8,000 m at 1430 UTC (Figure 10b). Simultaneously, LHR in the lower part of the cloud layer (≈ 2,000–4,000 m) intensifies, reaching maximum values of $MICR_{\theta_v} = 1.5\ K \cdot hr^{-1}$ in the lower part of the clouds at around 1430 UTC (Figure 13a). In parallel, the cloud dissolution adds up moisture in this layer, which caused a continuous increase in relative humidity between 3,000 and 5,000 m (e.g., by about 20% at 4,000 m height, Figure 13c) and reduction in evaporative cooling (Figure 13a). Moreover, the addition of moisture (Figure 13c) to the environment reduces the efficiency/extent of cloud dissolution by lateral entrainment processes. The dependence of the development of deep convection on the water-vapour content in the middle troposphere was also emphasised by, for example, Metzger *et al.* (2014). Shortly after that, that is, at about 1430 UTC, the entrainment-induced evaporative cooling diminishes (Figure 13a) and clouds deepen under enhanced advective warming (Figure 13b) in the layer around 5,000 m nearly. The precipitation falls continuously until about 1830 UTC in Δ_{156} (Figure 6).

4.4 | Cloud organisation

Concurrently with the changing of the microphysical cloud processes, the macrophysical cloud conditions like cloud size and cloud organisation are also subject to changes in the early afternoon, as obvious from Figure 14a,b. The diagram shows the mid-level cloud cover, that is, between ≈ 2,000 and 7,200 m. The growth of cloud size is attributed to cloud aggregation. The effect of cloud aggregation can be seen in the spatial distribution of mid-level cloud cover at 1500 UTC (Figure 14b), where aggregated clouds form mainly in the east and northeast of Berlin. The aggregated clouds extend up to

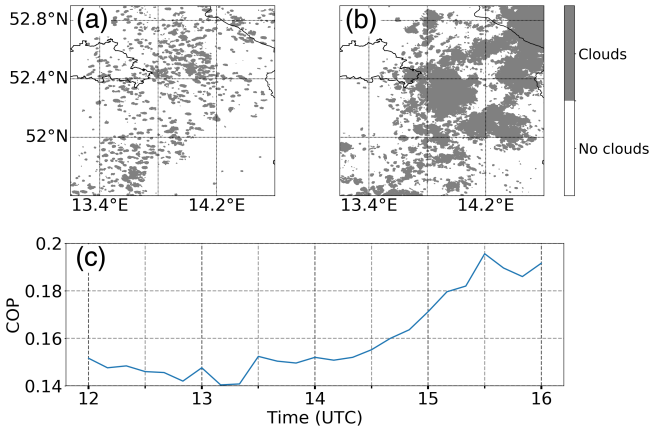

FIGURE 14 Mid-level cloud cover at (a) 1200 UTC and (b) 1500 UTC, and (c) COP for case study A1, July 26, 2012. The thin solid lines indicate the border of Berlin and the Germany–Poland border, respectively [Colour figure can be viewed at wileyonlinelibrary.com]

6,000 m. The aggregation was quantified using the COP of cloud cover (see Equation 2 in Section 2.4). Between 1200 and 1500 UTC, the COP value, which is averaged over a vertical layer from 1,000–5,000 m, increases from 0.14 to 0.17 (Figure 14c). We assume that, besides the decreased humidity between the clouds and their environment, the shift in cloud size towards larger clouds also reduces the cloud dissolution because of the reduced entrainment rate. The comparison of the properties of moist convection based on ICON-LEM simulations (model grid spacings of 625, 312, 156 m) in Pscheidt *et al.* (2019) and observations confirms that ICON simulations reproduce the organisation of convection reasonably well.

5 | DISCUSSION AND CONCLUSION

In this study, we investigated the impact of model grid spacing and LSR on clouds and convective precipitation for areas of different orographic complexities, that is, flat terrain, an isolated mountain range, and mountainous terrain. For each area, two days with weak synoptic forcing and scattered deep convection were selected. For these days, ICON simulations were performed using six model grid spacings: NWP (Δ_{5000}, Δ_{2500}) and LES (Δ_{1250}, Δ_{625}, Δ_{312}, and Δ_{156}) physics simulations in a nested set-up. Additionally, the impact of LSR on precipitation was deduced by using resolutions of land-surface properties and/or orography of 1,250 and 5,000 m, keeping the model grid spacing at 156 m.

Concerning the LES physics simulations from Δ_{1250} to Δ_{156}, convective clouds were formed in a time span of about 10 min, while the onset time of precipitation could differ by 0.5–2 hr (normally precipitation starts earlier in Δ_{1250} than Δ_{156}). While in Δ_{1250} a more spatially distributed precipitation pattern was generated, the precipitation became more aggregated with decreasing grid spacing. The results show that the areal mean daily precipitation amount for most of the cases decreases systematically across the model grid spacing. More specifically, the differences in the areal mean daily precipitation amount between the LES physics simulations (Δ_{1250}, Δ_{625}, Δ_{312}) and Δ_{156} normalised by Δ_{156} can be quite considerable, that is, the values are in the range of −26% to 400% with a 75th percentile of 155%. It is also found that the precipitation in Δ_{1250} is typically more intense in comparison with the finer LES physics simulations. These findings are consistent model behaviours found in the precipitation characteristics simulated for all cases. Compared with the RADOLAN-RW observations, the onset times of precipitation were closer to Δ_{1250}, but the precipitation patterns were more similar to the ones with finer grid spacing (Δ_{312} and Δ_{156}). Concerning the amount of precipitation, no clear hint concerning a grid spacing that fits the observations best is evident. Note that model validation is not the primary focus of this study.

The differences in areal mean daily precipitation amount due to modifications of the respective LSR are very small. The relative differences range from about −17% to 37% with a 75th percentile of 7% with a LSR of 1,250 m and increase to a range of −17% to 49% and a 75th percentile of 22% with a LSR of 5,000 m. These ranges hold for all types of land-surface sensitivity runs (L, O, and LO). Comparison of the sensitivity runs with Δ_{156} also shows that the onset of precipitation occurs at nearly the same time, and the precipitation patterns are in the same regions and show a more spatially clustered distribution. Finally, the intensities of precipitation in the sensitivity runs are very similar to Δ_{156}. This means that the impact of LSR on areal mean precipitation and even on precipitation patterns at a scales of hectometres and a few kilometres is much smaller than that of model grid spacing.

The comparison of precipitation between NWP (Δ_{2500}, Δ_{5000}) and the LES physics simulations (Δ_{156} to Δ_{1250}) shows that both considerably higher (A1 and A2) and lower (A3) values can occur. For one case in A3, Δ_{2500} and Δ_{5000} do not even generate precipitation at all, although precipitation exists in the LES physics simulations. Concerning the precipitation characteristics of the NWP physics simulations, it can be stated that they differ considerably with respect to the RADOLAN-RW observations. This includes the onset time of precipitation (too late), precipitation patterns (too isolated and too big), and precipitation amount (too high or too low).

To investigate whether this is due to model grid spacing or turbulence closure, both NWP and LES turbulence parameterization schemes were applied at Δ_{1250} and Δ_{625} in a test run (Singh, 2020). The comparison shows that already the transition from LES to NWP turbulence closure leads to considerably different precipitation behaviours and amounts. This means that the differences between the steps from LES (Δ_{1250}) and NWP (Δ_{2500}) simulations are caused by both the parameterization scheme and the model grid spacing.

The above findings pose the question of the factors and processes responsible for causing such large differences in precipitation across the model grid spacings (Δ_h). To answer this follow-up question, one case from A1 was selected that indicates quite substantial differences in precipitation characteristics between the LES physics simulations of Δ_{156} and Δ_{1250}. Differences already occur in the CBL conditions, with more unstable stratification in Δ_{1250} than in Δ_{156}. Such unrealistic unstable profiles at coarser model grid spacings, when applying the 3D Smagorinsky extended turbulence scheme, were found by Efstathiou and Beare (2015) and Simon *et al.* (2019), too. The different temperature profiles in Δ_{156} and Δ_{1250} also have consequences for the convection indices. Comparison of the cloud evolution and precipitation of Δ_{156} and Δ_{1250} reveals a similar onset time of CBL clouds but an earlier onset of precipitation in Δ_{1250} ($\approx$ 1200 UTC) than in Δ_{156} ($\approx$ 1400 UTC). Insight into the relevant reasons is gained by analysing the macrophysical cloud properties in combination with the heat and moisture budgets. We found that the model grid spacing impacts the macrophysical cloud properties directly. For example, at the beginning of cloud formation, a greater number of small and more scattered clouds are produced in Δ_{156} than in Δ_{1250}. The higher number of smaller clouds in Δ_{156} is likely related to the correspondingly smaller size and structure of the boundary-layer convergence fields (not shown). In subsequent hours, these CBL-based clouds grew deeper into the free troposphere in both grid spacings. However, while the thicker clouds in Δ_{1250} reached levels of 10,000 m and started to precipitate already by 1200 UTC, in Δ_{156} the cloud tops are restricted to approximately 5,500 m only. In Δ_{156}, according to the areal mean budget calculations, in the layer between 3,000 and 5,500 m the net temperature decrease is due to stronger evaporative cooling than advective warming. Inspecting a horizontal cross-section of the microphysics term at 4,000 m shows that the areal mean evaporative cooling is mainly generated by strong cooling at the edge and shell regions of small clouds. This eventually results in the dissolution of most of the clouds, in particular because this layer of the atmosphere is still quite dry. At midday, the dissolution of clouds even suppresses the precipitation in Δ_{156}, but simultaneously enhances the moisture in the corresponding layers where evaporation occurs. Later on, Δ_{156} cloud aggregation is an important factor with respect to the onset of precipitation: as soon as small clouds organise in clusters, evaporative cooling, which causes the dissolution of clouds by entrainment, reduces considerably and the clouds can grow deeper into the atmosphere. Subsequently, the cloud clusters result in precipitation, too. In previous studies, a different impact of model grid spacing on convection initiation and precipitation was observed. Keat *et al.* (2019) reported that convection initiation occurs slightly earlier when model resolution is reduced. Verrelle *et al.* (2015) observed an increase in precipitation with an increase in resolution, while Bryan and Morrison (2012) showed the opposite behaviour. We showed that the delayed onset of precipitation for higher model resolution was caused by evaporation of smaller clouds due to entrainment effects. The decisive impact of entrainment on small-sized dry and moist convection was also described by Morrison (2017) and Bryan and Morrison (2012). The effect obviously depends on the relative humidity in the mid-troposphere (Bryan and Morrison, 2012; Morrison, 2017). The simulation of too many small clouds in higher resolution models was assumed, for example, by Hanley *et al.* (2015). Whether both the enhanced cloud evaporation and the greater number of small clouds in Δ_{156} compared with Δ_{1250} are realistically simulated is crucial to know. The additional processes resolved at scales of hectometres, for example, lateral entrainment processes and their feedback on cloud evolution, need more attention in developing and testing different parameterization schemes. It was beyond the scope of this investigation to assess at which model grid spacing the entrainment processes are more realistic.

These research findings have crucial implications on weather prediction at scales from $\mathcal{O}$(100 m) to $\mathcal{O}$(5,000 m), to capture convective precipitation and be able to estimate its uncertainty as a function of model grid spacing and LSR. They also imply that, as the resolution of land-surface parameters has less impact on precipitation than the model grid spacing, this lower boundary data set is not necessarily needed at resolutions of up to $\mathcal{O}$(100 m).

ACKNOWLEDGEMENTS

This work was funded by the Federal Ministry of Education and Research (BMBF) in Germany as part of the research programme "High Definition Clouds and Precipitation for Climate Prediction–*HD*(*CP*)^2" (Förderkennzeichen (FKZ): 01LK1506E). Many thanks to Michael Kunz from KIT Karlsruhe for providing the lightning data. Open Access funding enabled and organized by Projekt DEAL.

CONFLICT OF INTEREST

The authors declare no conflict of interest.

ORCID

Shweta Singh https://orcid.org/0000-0003-0752-1952

REFERENCES

Adler, B., Kalthoff, N. and Gantner, L. (2011) Initiation of deep convection caused by land-surface inhomogeneities in West Africa: a modelled case study. *Meteorology and Atmospheric Physics*, 112, 15–27.

Adler, B., Kalthoff, N. and Gantner, L. (2017) Nocturnal low-level clouds over southern West Africa analysed using high-resolution simulations. *Atmospheric Chemistry and Physics*, 17, 899–910.

ASTER (2011). ASTER Global Digital Elevation Map Announcement. https://asterweb.jpl.nasa.gov/gdem.asp (accessed 20 August 2017).

Avissar, R. and Chen, F. (1993) Development and analysis of prognostic equations for mesoscale kinetic energy and mesoscale (subgrid scale) fluxes for large-scale atmospheric models. *Journal of the Atmospheric Sciences*, 50, 3751–3774.

Banta, R.M. (1990). The role of mountain flows in making clouds. In:, *Atmospheric Processes over Complex Terrain*: Boston, MA: Springer, pp. 229–283.

Bartels, H., Weigl, E., Reich, T., Lang, P., Wagner, A., Kohler, O. and Gerlach, N. (2004) Projekt RADOLAN–Routinever fahren zur Online-Aneichung der Radarniederschlagsdaten mit Hilfe von automatischen Bodenniederschlagsstationen (Ombrometer). *Deutscher Wetterdienst, Hydrometeorologie*, 5, 111.

Barthlott, C. and Hoose, C. (2015) Spatial and temporal variability of clouds and precipitation over Germany: multiscale simulations across the "gray zone". *Atmospheric Chemistry and Physics*, 15, 12361–12384.

Barthlott, C. and Kalthoff, N. (2011) A numerical sensitivity study on the impact of soil moisture on convection-related parameters and convective precipitation over complex terrain. *Journal of the Atmospheric Sciences*, 68, 2971–2987.

Berrisford, P., Dee, D., Poli, P., Brugge, R., Fielding, K., Fuentes, M., Kallberg, P., Kobayashi, S., Uppala, S. and Simmons, A. (2011). The ERA-Interim archive, Version 2.0. ERA Report Series 1, ECMWF, Shinfield Park, Reading.

Bradski, G. (2000) The OpenCV library. *Doctor Dobbs J*, 25, 120–125.

Bryan, G.H. and Morrison, H. (2012) Sensitivity of a simulated squall line to horizontal resolution and parameterization of microphysics. *Monthly Weather Review*, 140, 202–225.

Bryan, G.H., Wyngaard, J.C. and Fritsch, J.M. (2003) Resolution requirements for the simulation of deep moist convection. *Monthly Weather Review*, 131, 2394–2416.

Chow, F.K., Schär, C., Ban, N., Lundquist, K.A., Schlemmer, L. and Shi, X. (2019) Crossing multiple gray zones in the transition from mesoscale to microscale simulation over complex terrain. *Atmosphere*, 10, 274.

Chow, F.K., Weigel, A.P., Street, R.L., Rotach, M.W. and Xue, M. (2006) High-resolution large-eddy simulations of flow in a steep Alpine valley. Part I: methodology, verification, and sensitivity experiments. *Journal of Applied Meteorology and Climatology*, 45, 63–86.

Couvreux, F., Bazile, E., Canut, G., Seity, Y., Lothon, M., Lohou, F., Guichard, F. and Nilsson, E. (2016) Boundary-layer turbulent processes and mesoscale variability represented by numerical weather prediction models during the BLLAST campaign. *Atmospheric Chemistry and Physics*, 16, 8983–9002.

Cuxart, J. (2015) When can a high-resolution simulation over complex terrain be called LES? *Frontiers in Earth Science*, 3, 87.

Dee, D.P., Uppala, S.M., Simmons, A., Berrisford, P., Poli, P., Kobayashi, S., Andrae, U., Balmaseda, M., Balsamo, G., Bauer, P., Bechtold, P., Beljaars, A., van de Berg, L., Bidlot, J., Bormann, N., Delsol, C., Dragani, R., Fuentes, M., Geer, A., Haimberger, L., Healy, S., Hersbach, H., Hólm, E., Isaksen, L., Ka·llberg, P., Köhler, M., Matricardi, M., McNally, A., Monge-Sanz, B., Morcrette, J., Park, B., Peubey, C., de Rosnay, P., Tavolato, C., Thépaut, J. and Vitart, F. (2011) The ERA-Interim reanalysis: configuration and performance of the data assimilation system. *Quarterly Journal of the Royal Meteorological Society*, 137, 553–597.

Dipankar, A., Stevens, B., Heinze, R., Moseley, C., Zängl, G., Giorgetta, M. and Brdar, S. (2015) Large eddy simulation using the general circulation model ICON. *Journal of Advances in Modeling Earth Systems*, 7, 963–986.

Doswell III, C.A. and Rasmussen, E.N. (1994) The effect of neglecting the virtual temperature correction on CAPE calculations. *Weather and Forecasting*, 9, 625–629.

DWD-PAMORE (2015). PArallel MOdel data REtrieve from Oracle Databases (PAMORE). https://www.dwd.de/DE/leistungen/pamore/pamore.html. (accessed 20 May 2017).

Efstathiou, G. and Beare, R.J. (2015) Quantifying and improving sub-grid diffusion in the boundary-layer grey zone. *Quarterly Journal of the Royal Meteorological Society*, 141, 3006–3017.

Emanuel, K.A. (1994) *Atmospheric Convection*. Oxford: Oxford University Press.

Findell, K.L. and Eltahir, E.A. (1997) An analysis of the soil moisture–rainfall feedback, based on direct observations from Illinois. *Water Resources Research*, 33, 725–735.

Fiori, E., Parodi, A. and Siccardi, F. (2010) Turbulence closure parameterization and grid spacing effects in simulated supercell storms. *Journal of the Atmospheric Sciences*, 67, 3870–3890.

Fischer, G., Nachtergaele, F., Prieler, S., Van Velthuizen, H., Verelst, L. and Wiberg, D. (2008). Global agro-ecological zones assessment for agriculture (GAEZ 2008). International Institute for Applied Systems Analysis (IIASA), Laxenburg, Austria and Food and Agriculture Organization (FAO), Rome, Italy.

Gantner, L. and Kalthoff, N. (2010) Sensitivity of a modelled life cycle of a mesoscale convective system to soil conditions over West Africa. *Quarterly Journal of the Royal Meteorological Society*, 136, 471–482.

Gantner, L., Maurer, V., Kalthoff, N. and Kiseleva, O. (2017) The impact of land-surface parameter properties and resolution on the simulated cloud-topped atmospheric boundary layer. *Boundary-Layer Meteorology*, 165, 475–496.

GlobCover (2009). ESA GlobCover 2009 Project. Available at: http://due.esrin.esa.int/page_globcover.php. (accessed 20 August 2017).

Grams, C.M., Jones, S.C., Marsham, J.H., Parker, D.J., Haywood, J.M. and Heuveline, V. (2010) The Atlantic inflow to the Saharan heat low: observations and modelling. *Quarterly Journal of the Royal Meteorological Society*, 136, 125–140.

Hanley, K.E., Plant, R.S., Stein, T.H., Hogan, R.J., Nicol, J.C., Lean, H.W., Halliwell, C. and Clark, P.A. (2015) Mixing-length controls on high-resolution simulations of convective storms. *Quarterly Journal of the Royal Meteorological Society*, 141, 272–284.

Heim, C., Panosetti, D., Schlemmer, L., Leuenberger, D. and Schär, C. (2020) The influence of the resolution of orography on the simulation of orographic moist convection. *Monthly Weather Review*, 148, 2391–2410.

Heinze, R., Dipankar, A., Henken, C.C., Moseley, C., Sourdeval, O., Trömel, S., Xie, X., Adamidis, P., Ament, F., Baars, H., Barthlott, C., Behrendt, A., Blahak, U., Bley, S., Brdar, S., Brueck, M., Crewell, S., Deneke, H., Di Girolamo, P., Evaristo, R., Fischer, J., Frank, C., Friederichs, P., Göcke, T., Gorges, K., Hande, L., Hanke, M., Hansen, A., Hege, Hans-Christian, Hoose, C., Jahns, T., Kalthoff, N., Klocke, D., Kneifel, S., Knippertz, P., Kuhn, A., van Laar, T., Macke, A., Maurer, V., Mayer, B., I. Meyer, C., K. Muppa, S., A. J. Neggars, R., Orlandi, E., Pantillon, F., Pospichal, B., Röber, N., Scheck, L., Seifert, A., Seifert, P., Senf, F., Siligam, P., Simmer, C., Steinke, S., Stevens, B., Wapler, K., Weniger, M., Wulfmeyer, V., Zängl, G., Zhang, D. and Quaas, J. (2017) Large-eddy simulations over Germany using ICON: a comprehensive evaluation. *Quarterly Journal of the Royal Meteorological Society*, 143, 69–100.

Heise, E., Ritter, B. and Schrodin, R. (2006). Operational implementation of the multilayer soil model. Consortium for Small-Scale Modeling (COSMO) Technical Report 9, Deutscher Wetterdienst (DWD), Offenbach, Germany (accessed 20 August 2017).

Hohenegger, C., Schlemmer, L. and Silvers, L. (2015) Coupling of convection and circulation at various resolutions. *Tellus A*, 67, 26678.

Honnert, R. (2016) Representation of the grey zone of turbulence in the atmospheric boundary layer. *Advanced Science and Research*, 13, 63–67.

Honnert, R., Efstathiou, G.A., Beare, R.J., Ito, J., Lock, A., Neggers, R., Plant, R.S., Shin, H.H., Tomassini, L. and Zhou, B. (2020) The atmospheric boundary layer and the "gray zone" of turbulence: a critical review. *Journal of Geophysical Research*, 125(13), e2019JD030317.

Honnert, R. and Masson, V. (2014) What is the smallest physically acceptable scale for 1D turbulence schemes? *Frontiers in Earth Science*, 2, 27.

Imamovic, A., Schlemmer, L. and Schär, C. (2017) Collective impacts of orography and soil moisture on the soil moisture-precipitation feedback. *Geophysical Research Letters*, 44, 11–682.

Kalthoff, N., Fiedler, F., Kohler, M., Kolle, O., Mayer, H. and Wenzel, A. (1999) Analysis of energy balance components as a function of orography and land use and comparison of results with the distribution of variables influencing local climate. *Theoretical and Applied Climatology*, 62, 65–84.

Kalthoff, N., Kohler, M., Barthlott, C., Adler, B., Mobbs, S., Corsmeier, U., Träumner, K., Foken, T., Eigenmann, R., Krauss, L., Khodayar, S. and Di Girolamo, P. (2011) The dependence of convection-related parameters on surface and boundary-layer conditions over complex terrain. *Quarterly Journal of the Royal Meteorological Society*, 137, 70–80.

Keat, W.J., Stein, T.H., Phaduli, E., Landman, S., Becker, E., Bopape, M.-J.M., Hanley, K.E., Lean, H.W. and Webster, S. (2019) Convective initiation and storm life cycles in convection-permitting simulations of the Met Office Unified Model over South Africa. *Quarterly Journal of the Royal Meteorological Society*, 145, 1323–1336.

Kirshbaum, D.J., Adler, B., Kalthoff, N., Barthlott, C. and Serafin, S. (2018) Moist orographic convection: physical mechanisms and links to surface-exchange processes. *Atmosphere*, 9, 80.

Koster, R.D., Dirmeyer, P.A., Guo, Z., Bonan, G., Chan, E., Cox, P., Gordon, C., Kanae, S., Kowalczyk, E., Lawrence, D., Liu, P., Lu, C., Malyshev, S., McAvaney, B., Mitchell, K., Mocko, D., Oki, T., Oleson, K., Pitman, A., Sud, Y.C., Taylor, C. M., Verseghy, D., Vasic, R., Xue, Y. and Yamada, T. (2004) Regions of strong coupling between soil moisture and precipitation. *Science*, 305, 1138–1140.

Kottmeier, C., Kalthoff, N., Barthlott, C., Corsmeier, U., Van Baelen, J., Behrendt, A., Behrendt, R., Blyth, A., Coulter, R., Crewell, S., di Girolamo P., Dorninger, M., Flamant, C., Foken, T., Hagen, M., Hauck, C., Höller, H., Konow, H., Kunz, M., Mahlke, H., Mobbs, S., Richard, E., Steinacker, R., Weckwerth, T., Wieser, A. and Wulfmeyer, V. (2008) Mechanisms initiating deep convection over complex terrain during COPS. *Meteorologische Zeitschrift*, 17, 931–948.

Leary, L.A. and Ritchie, E.A. (2009) Lightning flash rates as an indicator of tropical cyclone genesis in the eastern North Pacific. *Monthly Weather Review*, 137, 3456–3470.

Lilly, D.K. (1962) On the numerical simulation of buoyant convection. *Tellus*, 14, 148–172.

Metzger, J., Barthlott, C. and Kalthoff, N. (2014) Impact of upstream flow conditions on the initiation of moist convection over the island of Corsica. *Atmospheric Research*, 145, 279–296.

Mlawer, E.J., Taubman, S.J. and Clough, S.A. (1995). RRTM: a Rapid Radiative Transfer Model. In:, *Conference on Atmospheric Transmission Models, 6–8 June 1995*, Bedford, Massachusetts, United States: Phillips Laboratory, 150–157.

Morrison, H. (2016) Impacts of updraft size and dimensionality on the perturbation pressure and vertical velocity in cumulus convection. Part I: simple, generalized analytic solutions. *Journal of the Atmospheric Sciences*, 73, 1441–1454.

Morrison, H. (2017) An analytic description of the structure and evolution of growing deep cumulus updrafts. *Journal of the Atmospheric Sciences*, 74, 809–834.

Morton, B., Taylor, G.I. and Turner, J.S. (1956) Turbulent gravitational convection from maintained and instantaneous sources. *Proceedings of the Royal Society of London. Series A, Mathematical and Physical Sciences*, 234, 1–23.

Pal, J.S. and Eltahir, E.A. (2001) Pathways relating soil moisture conditions to future summer rainfall within a model of the land–atmosphere system. *Journal of Climate*, 14, 1227–1242.

Prill, F. (2014) *DWD ICON Tools Documentation*. Offenbach, Germany: Deutscher Wetterdienst (DWD).

Pscheidt, I., Senf, F., Heinze, R., Deneke, H., Trömel, S. and Hohenegger, C. (2019) How organized is deep convection over Germany? *Quarterly Journal of the Royal Meteorological Society*, 145, 2366–2384.

Raschendorfer, M. (2001a) The new turbulence parameterization of LM. *COSMO Newsletter*, 1, 89–97. http://www.cosmo-model.org/content/model/documentation/newsLetters/newsLetter01/newsLetter_01.pdf

Raschendorfer, M. (2001b) The new turbulence parameterization of LM. *COSMO Newsletter*, 1, 89–97.

Rotach, M.W., Stiperski, I., Fuhrer, O., Goger, B., Gohm, A., Obleitner, F., Rau, G., Sfyri, E. and Vergeiner, J. (2017) Investigating exchange processes over complex topography: the Innsbruck Box (i-Box). *Bulletin of the American Meteorological Society*, 98, 787–805.

Schär, C., Lüthi, D., Beyerle, U. and Heise, E. (1999) The soil–precipitation feedback: a process study with a regional climate model. *Journal of Climate*, 12, 722–741.

Schrodin, R. and Heise, E. (2002) A new multilayer soil model. *COSMO Newsletter*, 2, 149–151.

Schulz, W., Diendorfer, G., Pedeboy, S. and Poelman, D.R. (2016) The European lightning location system EUCLID–Part 1: performance analysis and validation. *Natural Hazards and Earth System Sciences*, 16, 595–605.

Seifert, A. and Beheng, K.D. (2006) A two-moment cloud microphysics parameterization for mixed-phase clouds. Part 1: model description. *Meteorology and Atmospheric Physics*, 92, 45–66.

Shuttleworth, W.J. (1991). Evaporation models in hydrology. In:, *Land Surface Evaporation*. New York: Springer, pp. 93–120.

Simon, J.S., Zhou, B., Mirocha, J.D. and Chow, F.K. (2019) Explicit filtering and reconstruction to reduce grid dependence in convective boundary layer simulations using WRF-LES. *Monthly Weather Review*, 147, 1805–1821.

Singh, S. (2020) *Convective Precipitation Simulated with ICON over Heterogeneous Surfaces in Dependence on Model and Land-surface Resolution*. Karlsruhe: Karlsruhe Institute of Technology (KIT).

Smagorinsky, J. (1963) General circulation experiments with the primitive equations: I. The basic experiment. *Monthly Weather Review*, 91, 99–164.

Sommeria, G. and Deardorff, J. (1977) Subgrid-scale condensation in models of nonprecipitating clouds. *Journal of the Atmospheric Sciences*, 34, 344–355.

Stevens, B., Acquistapace, C., Hansen, A., Heinze, R., Klinger, C., Klocke, D., Schubotz, W., Windmiller, J., Adamidis, P., Arka, I., Barlakas, V., Biercamp, J., Brueck, M., Brune, S., Buehler, S., Burkhardt, U., Cioni, G., Costa-Suros, M., Crewell, S., Crüger, S., Deneke, H., Friedrichs, P., Henken, C., Hohenegger, C., Jacob, M., Jakub, F., Kalthoff, N., Köhler, M., Van Laar, T., Li, P., Löhnert, U., Macke, A., Madenbach, N., Mayer, B., Nam, C., Naumann, A., Peters, K., Poll, S., Quaas, J., Röber, N., Rochetin, N., Scheck, L., Schemann, V., Schnitt, S., Seifert, A., Senf, F., Shapkalijevski, M., Simmer, C., Singh, S., Sourdeval, O., Spickermann, D., Strandgren, J., Tessiot, O., Vercauteren, N., Vial, J., Voigt, A. and Zängl, G. (2020) The added value of large-eddy and storm-resolving models for simulating clouds and precipitation. *Journal of the Meteorological Society of Japan*, 98, 395–435.

Stull, R.B. (1988) *An Introduction to Boundary Layer Meteorology* Vol. 13. Dordrecht: Kluwer Academic Publication.

Taylor, C.M., Parker, D.J. and Harris, P.P. (2007) An observational case study of mesoscale atmospheric circulations induced by soil moisture. *Geophysical Research Letters*, 34, L15801.

Tompkins, A.M. (2002) A prognostic parameterization for the subgrid-scale variability of water vapor and clouds in large-scale models and its use to diagnose cloud cover. *Journal of the Atmospheric Sciences*, 59, 1917–1942.

Turner, J. (1963) The motion of buoyant elements in turbulent surroundings. *Journal of Fluid Mechanics*, 16, 1–16.

Varble, A., Morrison, H. and Zipser, E. (2020) Effects of under-resolved convective dynamics on the evolution of a squall line. *Monthly Weather Review*, 148, 289–311.

Verrelle, A., Ricard, D. and Lac, C. (2015) Sensitivity of high-resolution idealized simulations of thunderstorms to horizontal resolution and turbulence parametrization. *Quarterly Journal of the Royal Meteorological Society*, 141, 433–448.

Weckwerth, T.M. (2000) The effect of small-scale moisture variability on thunderstorm initiation. *Monthly Weather Review*, 128, 4017–4030.

Weisman, M.L., Skamarock, W.C. and Klemp, J.B. (1997) The resolution dependence of explicitly modeled convective systems. *Monthly Weather Review*, 125, 527–548.

Western, A.W., Grayson, R.B. and Blöschl, G. (2002) Scaling of soil moisture: a hydrologic perspective. *Annual Review of Earth and Planetary Sciences*, 30, 149–180.

White, B., Buchanan, A., Birch, C., Stier, P. and Pearson, K. (2018) Quantifying the effects of horizontal grid length and parameterized convection on the degree of convective organization using a metric of the potential for convective interaction. *Journal of the Atmospheric Sciences*, 75, 425–450.

Wyngaard, J.C. (2004) Toward numerical modeling in the "Terra Incognita". *Journal of the Atmospheric Sciences*, 61, 1816–1826.

Zängl, G., Reinert, D., Rípodas, P. and Baldauf, M. (2015) The ICON (ICOsahedral Non-hydrostatic) modelling framework of DWD and MPI-M: description of the non-hydrostatic dynamical core. *Quarterly Journal of the Royal Meteorological Society*, 141, 563–579.

Zhou, B., Simon, J.S. and Chow, F.K. (2014) The convective boundary layer in the Terra Incognita. *Journal of the Atmospheric Sciences*, 71, 2545–2563.

How to cite this article: Singh S, Kalthoff N, Gantner L. Sensitivity of convective precipitation to model grid spacing and land-surface resolution in ICON. *Q.J.R. Meteorol. Soc.*. 2021;1–20. https://doi.org/10.1002/qj.4046